

# Role of Thermal and Non-thermal Processes in the ISM of Magellanic Clouds

H. Hassani<sup>1,2\*</sup>, F. Tabatabaei<sup>2</sup>, A. Hughes<sup>3,4</sup>, J. Chastenet<sup>5,6</sup>, A. F. McLeod<sup>7,8</sup>,

E. Schinnerer<sup>9</sup>, S. Nasiri<sup>1</sup>,

<sup>1</sup> *Shahid Beheshti University, Faculty of Physics, Department of Astronomy and Astrophysics, Tehran, Iran, 19839*

<sup>2</sup> *School of Astronomy, Institute for Research in Fundamental Sciences (IPM), PO Box 19395-5531, Tehran, Iran*

<sup>3</sup> *CNRS, IRAP, 9 Av. du Colonel Roche, BP 44346, F-31028 Toulouse cedex 4, France*

<sup>4</sup> *Université de Toulouse, UPS-OMP, IRAP, F-31028 Toulouse cedex 4, France*

<sup>5</sup> *Center for Astrophysics and Space Sciences, Department of Physics, University of California, San Diego, 9500 Gilman Drive, La Jolla, CA 92093, USA*

<sup>6</sup> *Sterrenkundig Observatorium, Ghent University, Krijgslaan 281-S9, 9000 Gent, Belgium*

<sup>7</sup> *Department of Astronomy, University of California Berkeley, Berkeley, CA 94720, USA*

<sup>8</sup> *Centre for Extragalactic Astronomy, Department of Physics, Durham University, South Road, Durham DH1 3LE, UK*

<sup>9</sup> *Max-Planck-Institut für Astronomie, Königstuhl 17, D-69117, Heidelberg, Germany*

Last updated 2021 October 31

## ABSTRACT

The radio continuum emission is a dust-unbiased tracer of both the thermal and non-thermal processes in the interstellar medium. We present new maps of the free-free and synchrotron emission in the Magellanic Clouds (MCs) at 0.166, 1.4, and 4.8 GHz with no prior assumption about the radio non-thermal spectrum. The maps were constructed using a de-reddened H $\alpha$  map as a template for the thermal radio emission, which we subtract from maps of the total radio continuum emission. To de-redden the H $\alpha$  emission, it is important to know the fraction of dust surface density that attenuates the H $\alpha$  emission along the line-of-sight,  $f_d$ . This fraction is obtained by comparing the dust opacity obtained through the infrared emission spectrum and the Balmer decrement method. In star-forming regions, the median  $f_d$  is about 0.1 which is by a factor of 3 lower than that in diffuse regions. We obtain a global thermal radio fraction,  $f_{th}$ , of 30 per cent (35 per cent) in the LMC (SMC) at 1.4 GHz. Furthermore, we present maps of the equipartition magnetic field strength with average values of  $\simeq 10.1 \mu\text{G}$  in the LMC and  $\simeq 5.5 \mu\text{G}$  in the SMC. The magnetic field is proportional to the star formation rate to a power of 0.24 and 0.20 for the LMC and SMC, respectively. This study shows that the non-thermal processes control the interstellar medium in the MCs.

**Key words:** radio continuum, ISM, Magellanic Clouds, thermal, non-thermal, cosmic rays.

## 1 Introduction

The radio continuum (RC) emission observed from astrophysical sources is dominated by the non-thermal (synchrotron) and the thermal (free-free) emission at frequencies  $\lambda < 10$  GHz (Condon 1992). The thermal emission originates from the warm ionized nebular medium (e.g., H II regions) with a typical electron temperature of  $T_e \simeq 10^4$  K and has often a flat power-law radio spectral energy distribution  $S_\nu = \nu^{-0.1}$  (e.g., Filipovic et al. 1998; Draine 2011). The non-thermal emission is due to cosmic-ray electrons (CREs) accelerated by the magnetic field in the interstellar medium (e.g., supernova remnants) and is described by a power-law spectrum with a variable non-thermal spectral index  $\alpha_n$  ( $S_\nu = \nu^{\alpha_n}$ ). Interaction and energy loss of CREs in different

environments (e.g., spiral arms of galaxies or their nuclei) change the non-thermal spectral index  $\alpha_n$  (Longair 2011). Hence, assuming a constant  $\alpha_n$  in resolved studies can underestimate or overestimate the synchrotron emission depending on the medium. For instance, assuming  $\alpha_n = -1$  results in an underestimation of both the non-thermal emission (by  $> 30$  per cent Tabatabaei et al. 2007) and the magnetic field strength in massive star-forming regions. Avoiding such assumptions, several attempts have been made to map the pure synchrotron emission in nearby galaxies, including M 33, M 31, NGC 6946, and NGC 1097 (Tabatabaei et al. 2013b; Tabatabaei et al. 2013a, 2018). Separating the thermal and non-thermal emission is the first step towards understanding the origin of the well-known correlation between the RC and infrared (IR) continuum emission in galaxies (van der Kruit 1971; de Jong et al. 1985; Helou et al. 1985). It is also vital in studying the energy balance and structure formation in the interstellar medium (ISM) of galaxies.

\* E-mail: hamid@ipm.ir

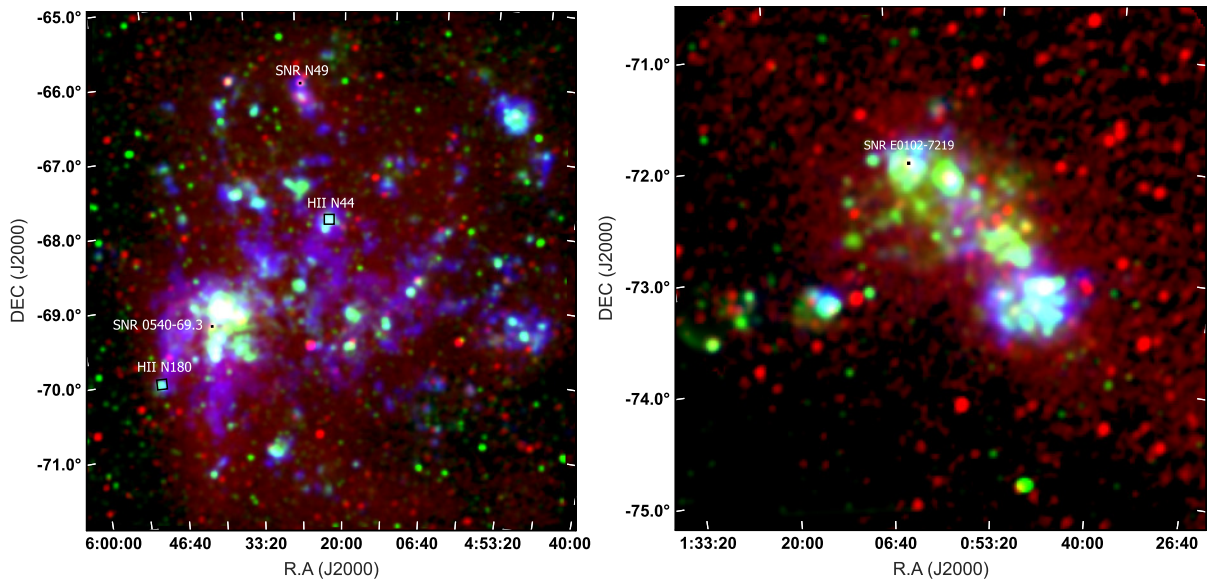


**Figure 1.** Three-colour composite images of the Large Magellanic Cloud (*left*) and the Small Magellanic Cloud (*right*) showing the radio continuum emission at 0.166 GHz from the GLEAM survey in log scale (*red*), the H $\alpha$  emission from the MCELS survey in linear scale (*green*), and the dust mass surface density from Chastenot et al. (2019) in log scale (*blue*). Black squares show the MUSE/VLT observed fields.

The MCs, our nearest neighbour galaxies, provide ideal laboratories for detailed ISM studies in low-mass and low-metallicity systems. The Large Magellanic Cloud (LMC) is at a distance of 49.9 kpc (Pietrzyński et al. 2019) with an almost face-on view that hosts one of the brightest and complex extragalactic H II regions, 30 Doradus (hereafter 30 Dor). Being located at about 62.4 kpc from our Sun (Graczyk et al. 2020), the Small Magellanic Cloud (SMC) is farther away and more inclined ( $i = 64^\circ$ , see e.g., Subramanian & Subramanian 2015) than the LMC. These inclinations mean that the distances reported can change up to 10 per cent from one end to other end of each galaxy. General properties of the MCs are summarized in Table 1.

They have been extensively studied in RC in both total power (For et al. 2018; Klein et al. 1989; Loiseau et al. 1987; Haynes et al. 1991; Joseph et al. 2019; Pennock et al. 2021) and polarization (Gaensler et al. 2005; Mao et al. 2008; Mao et al. 2012; Klein et al. 1993). The Herschel space observatory and the Spitzer space telescope have made major breakthroughs in studies of the dust and gas in the MCs (Gordon et al. 2011; Meixner et al. 2006, 2013; Lakićević et al. 2015). Moreover, nebular emission lines maps from both the LMC and the SMC are available through optical observations such as the Magellanic Clouds Emission Line Survey (MCELS; Smith & MCELS Team 1999; Smith et al. 2005; Points et al. 2005; Winkler et al. 2015; Pellegrini et al. 2012).

Several attempts have been made to study the RC emission components in the MCs, mostly using a fixed  $\alpha_n$  across the galaxies (hereafter classical separation method). Klein et al. (1989) obtained  $\alpha_n = -0.84$  and found a thermal fraction of  $f_{\text{th}} = 55$  per cent at 1.4 GHz for the LMC. Hughes et al. (2006) studied the radio-IR correlation separately for the thermal and non-thermal RC assuming  $\alpha_n = -0.7$  and found a tight correlation in regions with a high thermal fraction.

The structure and strength of the magnetic fields in the

**Table 1.** General parameters adopted for the MCs.

LMC	
Centre (J2000)	RA = $05^{\text{h}} 23^{\text{m}} 34^{\text{s}}$ Dec = $-69^\circ 45' 22''$
Inclination <sup>1</sup>	$34.0^\circ$
Distance <sup>2</sup>	49.9 kpc ( $1'' = 0.24$ pc)
SMC	
Centre (J2000)	RA = $00^{\text{h}} 52^{\text{m}} 44^{\text{s}}$ Dec = $-72^\circ 49' 42''$
Inclination <sup>3</sup>	$64.4^\circ$
Distance <sup>4</sup>	62.4 kpc ( $1'' = 0.30$ pc)

References: <sup>1</sup> van der Marel & Kallivayalil 2014. <sup>2</sup> Pietrzyński et al. 2019. <sup>3</sup> Subramanian & Subramanian 2015. <sup>4</sup> Graczyk et al. 2020.

MCs have been studied by several authors (Klein et al. 1993; Gaensler et al. 2005; Mao et al. 2008; Mao et al. 2012). In the LMC, an average magnetic field along the line of sight of  $\simeq 4.3 \mu\text{G}$  was obtained through Faraday rotation studies (Gaensler et al. 2005). Using the classical thermal/non-thermal separation technique, (Klein et al. 1989) reported an equipartition field strength of  $\simeq 6 \mu\text{G}$  in the same galaxy. In the SMC, Mao et al. (2008) found a galactic-scale mean field strength of  $\simeq 0.2 \mu\text{G}$  along the line of sight and a random field strength of  $\simeq 3 \mu\text{G}$  in the sky plane. However, no full map of the magnetic field strength in the MCs is available to study its role in the ISM energy balance and structure formation. The ordered magnetic field is shown to be smaller in dwarf galaxies than in spiral galaxies (Chyży et al. 2011) indicating a large-scale dynamo process may not maintain the production of the magnetic field in dwarf galaxies. As the small-scale dynamo originates from the injection of turbulent energy from supernova explosions, massive stars may play a primary role in dwarf galaxies such as the MCs. Such a small-scale dynamo can be investigated through its power-law relation with star formation (Schleicher & Beck 2013). Chyży et al. (2011) finds such correlations for dwarf galaxies in global studies. Mapping the magnetic field strength is

needed to address those relations in the MCs, taking advantage of our close distance to the MCs and hence inspecting these questions in the physical resolution of less than 80 pc for the first time.

The paper aims to study the thermal and non-thermal properties of the ISM, map the total magnetic field strength, and investigate its correlation with SFR in the MCs. Using recent Murchison Widefield Array (Lonsdale et al. 2009; Bowman et al. 2013; Tingay et al. 2013) low-frequency observations as well as archival ATCA and Parkes data (Kim et al. 1998; Kim et al. 2003; Haynes et al. 1986; Filipovic et al. 1995, 1996a, 1997), we present full maps of the thermal and non-thermal emission for both the LMC and the SMC.

Unlike the classical separation method, we do not assume a fixed  $\alpha_n$  to obtain the thermal and non-thermal RC maps. We use the Thermal Radio Template (TRT) technique developed for NGC 6946 (Tabatabaei et al. 2013a). This method uses a recombination line such as H $\alpha$  emission to trace the thermal free-free emission. In this work, to de-redden the H $\alpha$  emission, no assumption for the fraction of dust attenuating the emission ( $f_d$ ) is applied unlike our previous studies. We determine  $f_d$  for the MCs by comparing the dust mass obtained using the Balmer-line-decrement ratio method (e.g., Cardelli et al. 1989; Calzetti et al. 2000) with that extracted from the dust emission Spectral Energy Distribution (SED) studies. Hence, this paper presents distributions of the thermal and non-thermal RC emission across the MCs more precisely than before.

The data is described in Section 2. In Section 3, we determine  $f_d$  for a sample of H II regions as well as for more diffuse regions and present a general  $f_d$  calibration relation using its correlation with the neutral gas. In Section 4, we present the thermal and non-thermal maps at different frequencies at an angular resolution of  $221''$  ( $\sim 53$  pc) for the LMC and  $235''$  ( $\sim 71$  pc) for the SMC. The non-thermal spectral index maps are presented in Section 5. After mapping the magnetic field strength, we investigate its correlation with the star formation rate (SFR) at different spatial resolutions, compare the thermal and non-thermal energy densities of the ISM, and discuss the propagation of CREs in Section 6.

## 2 Data

The data used in this study are summarised in Table 2. The MCs were observed with the Murchison Widefield Array telescope (Lonsdale et al. 2009; Tingay et al. 2013) as part of the GaLactic Extragalactic All-sky MWA (GLEAM) survey in the frequency range of 0.074-0.231 GHz (Wayth et al. 2015). The data reduction is explained in detail by Hurley-Walker et al. (2016). Due to slight changes in ionospheric conditions, a point spread function (PSF) map is created for each mosaic with a variation of 15-20 per cent across each field. We used radio continuum at 0.166 GHz with a robust 0 weighting from For et al. (2018). Calibration uncertainty in the flux density is 8.5 per cent for the LMC and 13 per cent for the SMC (Hurley-Walker et al. 2016).

At higher frequencies, the LMC and the SMC have been observed with the Australia Telescope Compact Array (ATCA) and Parkes telescope at 1.4 GHz and 4.8 GHz by several authors (Hughes et al. 2007; Dickel et al. 2005; Dickel et al. 2010; Wong et al. 2011a; Crawford et al. 2011). For the LMC, we

used the merged ATCA+Parkes data at 1.4 GHz and 4.8 GHz as presented by Hughes et al. (2007) and Dickel et al. (2005), respectively. We assume a calibration uncertainty of 6.5 per cent at 1.4 GHz and 8.5 per cent at 4.8 GHz for the LMC data. For the SMC, we used these observations only at 1.4 GHz assuming a 5 per cent calibration uncertainty (Wong et al. 2011a). The quality and signal-to-noise ratio of the available RC data of the SMC are much poorer at 4.8 GHz (Dickel et al. 2010; Crawford et al. 2011) than at 1.4 GHz. The RMS noise value of the RC map is about 2.6 times higher at 4.8 GHz than at 1.4 GHz. We note that, in the SMC, the signal-to-noise ratio is by a factor of 2 lower than that in the LMC at 4.8 GHz. These data are also severely affected by artefacts around bright sources. These prevent studying low-surface brightness regions of the SMC that is the main interest of this study. Hence, we opt not to use these data at 4.8 GHz for the SMC.

The H $\alpha$  map of the MCs was taken through the MCELS survey (Winkler et al. 2015; Smith & MCELS Team 1999). This survey covers the central  $8^\circ \times 8^\circ$  of the LMC and  $4.5^\circ \times 3.5^\circ$  of the SMC. It used a Curtis Schmidt telescope with a pixel size of  $2.3''$  (Smith & MCELS Team 1999). The H $\alpha$  maps were continuum subtracted for the entire mosaic, rather than field-by-field using two continuum band filters as detailed in Paredes et al. (2015). We masked several bright background point sources with H $\alpha$  flux of about 100 times higher than in H II regions as they seem to be suffering from saturation in the reduction process. We use a calibration uncertainty of 10 per cent for the H $\alpha$  maps provided by the MCELS Team (private communication).

Absolute photometry of H $\alpha$  and H $\beta$  for 74 (27) H II regions in the LMC (SMC) has been reported by Caplan & Deharveng (1985); Caplan et al. (1996) (hereafter Caplan catalog). Photometry measurements were taken in circular apertures of  $4.89'$ ,  $2.00'$ , and  $1.06'$  diameter. These aperture sizes are adopted to ensure integration over the whole H II regions and for comparison with Parkes radio continuum at 4.8 GHz data. The LMC H $\alpha$ /H $\beta$  flux ratio and their emission lines suffer from 4 per cent uncertainty in random errors, imprecise atmospheric attenuation, and other systematic errors. However, the uncertainty in the H $\alpha$ /H $\beta$  flux ratio is estimated to be about 7 per cent in the SMC (Caplan & Deharveng 1985; Caplan et al. 1996).

The MCs were observed with Herschel and Spitzer in different bands from  $3.6 \mu\text{m}$  to  $500 \mu\text{m}$  by the HERITAGE and SAGE projects (Meixner et al. 2006, 2010, 2013, 2015; Gordon et al. 2011). Chastenet et al. (2019) modelled the FIR dust emission using the Draine & Li (2007) dust model. We use their total dust mass surface density maps with an angular resolution of  $36''$ .

The 21-cm H I line emission was observed with ATCA and Parkes (Kim et al. 2003) and the CO (1-0) line emission is provided by the Magellanic Mopra Assessment (MAGMA) survey (Wong et al. 2011b, 2017) for the LMC.

We use optical IFU MUSE/VLT observations toward several fields in the MCs (see Fig. 1), including H II regions and Supernova remnants (SNRs) to investigate the extinction properties of the diffuse gas in SNRs vs star-forming regions. These data were taken by Wide Field Mode (WFM) with a FoV  $\approx 1'$  and are summarized in Table 3. The two H II regions of the LMC are reduced and mosaiced by McLeod et al. (2018). Our sample of MUSE SNRs fields was taken

**Table 2.** Images of the Magellanic Clouds used in this study.

Frequency	Angular Resolution (arcsec)	RMS	Ref.	Telescope
LMC				
0.166 GHz	221 × 221	0.02 (Jy beam <sup>-1</sup> )	For et al. (2018)	MWA
1.4 GHz	40 × 40	0.30 (mJy beam <sup>-1</sup> )	Hughes et al. (2007)	ATCA+Parkes
4.8 GHz	33 × 33	0.30 (mJy beam <sup>-1</sup> )	Dickel et al. (2005)	ATCA+Parkes
6563 Å (Hα)	4.6 × 4.6	0.12 (10 <sup>-15</sup> erg s <sup>-1</sup> cm <sup>2</sup> )	Smith & MCELS Team (1999)	UM/CTIO
70 μm	18 × 18	0.41 (MJy sr <sup>-1</sup> )	Meixner et al. (2006)	Spitzer/MIPS
CO (1-0)	45 × 45	0.40 (K km s <sup>-1</sup> )	Wong et al. (2017, 2011b)	Mopra
H I - 21 cm	60 × 60	15 (mJy beam <sup>-1</sup> )	Kim et al. (2003)	ATCA+Parkes
4800-9300 Å (IFU)	≈ 0.4 × 0.4	-	Bacon et al. (2010)	MUSE/VLT
SMC				
0.166 GHz	235 × 235	0.02 (Jy beam <sup>-1</sup> )	For et al. (2018)	MWA
1.4 GHz	98 × 98	1.50 (mJy beam <sup>-1</sup> )	Wong et al. (2011a)	ATCA+Parkes
6563 Å (Hα)	4.6 × 4.6	0.01 (10 <sup>-17</sup> erg s <sup>-1</sup> cm <sup>2</sup> )	Smith & MCELS Team (1999)	UM/CTIO
70 μm	18 × 18	0.47 (MJy sr <sup>-1</sup> )	Gordon et al. (2011)	Spitzer/MIPS
4800-9300 Å (IFU)	≈ 0.4 × 0.4	-	Bacon et al. (2010)	MUSE/VLT

**Table 3.** MUSE/VLT observed fields in the MCs.

Name	R.A. (J2000)	DEC (J2000)	Area	Program ID	Ref.
LMC/N44	80.534	-67.936	8' × 8'	096.C-0137(A)	McLeod et al. (2018)
LMC/N49	81.505	-66.083	60'' × 60''	0100.D-0037(A)	Van Loon, J.T <sup>1</sup>
LMC/SNR 0540-69.3	85.046	-69.332	60'' × 60''	0102.D-0769(A)	Lyman, Joseph <sup>1</sup>
LMC/N180	87.206	-70.055	8' × 8'	096.C-0137(A)	McLeod et al. (2018)
SMC/1E0102-7219	16.012	-72.031	60'' × 60''	297.D-5058(A)	Vogt et al. (2017) <sup>1</sup>

<sup>1</sup> Data retrieved from the ESO Phase 3 Archive.

from the Phase 3 ESO Science Archive and reduced using ESO's automatic pipeline (Weilbacher et al. 2016). We note that this automatic pipeline may over-subtract emission lines and produce artificial absorption lines in the spectrum. Comparing MUSE SNRs Hα flux with MCELS survey data in 1' rectangular aperture shows an agreement within <18 per cent of total flux. We take extra 20 per cent uncertainty in flux of emission line ratio ( $F_{H\alpha}/F_{H\beta}$ ) for the sky over-subtraction effect in the LMC SNRs. We did not find any noticeable absorption lines in the integrated spectra or each pixel of the SNR 1E0102-7219.

All maps were convolved to the lowest common resolution of our datasets, 221'' × 221'' for the LMC and 235'' × 235'' for the SMC using Gaussian kernels. The smoothed maps were then regridded to a common astrometric grid. We considered not only the RMS noise ( $\sigma_{\text{rms}}$ ) of the observed maps, but also the calibration uncertainty ( $\sigma_{\text{cal}}$ ) of the instruments to estimate uncertainties in fluxes (following  $\sigma = \sqrt{\sigma_{\text{rms}}^2 + \sigma_{\text{cal}}^2}$ ). These errors were then propagated to obtain uncertainties in other parameters reported throughout the paper.

### 3 Extinction in the Magellanic Clouds

The Herschel and Spitzer space telescopes have made a major breakthrough in mapping the dust content of galaxies. These observations can be used to map extinction and de-redden the optical Hα emission provided that the relative distribution of emitting sources and dust particles is known along the line of sight (Tabatabaei et al. 2013a). A uniform mix of dust and ionized gas emitting Hα requires half of the total dust mass (or optical depth) to be considered in de-reddening. A

smaller fraction must be used in the more realistic case of non-uniformity, such as a smaller z-distribution of dust than ionized gas (Dickinson et al. 2003) or due to clumpiness. As follows, the total dust opacity is first obtained in the MCs. Then we derive the fraction of it that is linked to reddening of the Hα emission ( $f_d$ ) by comparing the total dust optical depth with true extinction obtained using the Hα-to-Hβ ratio method. This is done for H II regions and a few MUSE fields including more diffuse ISM. Moreover, a calibration relation for  $f_d$  is obtained by investigating its correlation with neutral gas surface density across the LMC.

#### 3.1 Dust opacity

Using the Herschel and Spitzer data, Chasten et al. (2019) mapped different dust properties including dust mass surface density in the MCs based on the DL07 model (Draine & Li 2007). A composition of carbonaceous and amorphous silicates were assumed for dust grains which are heated by a variable radiation field  $U$  with a delta-function distribution. Taking a fixed  $U_{\text{max}} = 10^7 U_{\odot}$ , the minimum interstellar radiation field intensity spans a range of  $0.1 U_{\odot} \leq U_{\text{min}} < 50 U_{\odot}$ . Considering the Galactic  $R_V = 3.1$  (Cardelli et al. 1989), dust SEDs were fitted based on this model from 3.6 to 500 μm. This results in 36'' resolution maps of dust mass surface density  $\Sigma_d$  with a pixel size of 14'' for the MCs. This leads to a dust optical depth following  $\tau_{\text{dust}} = \kappa_{\Sigma} \Sigma_d$ , where  $\kappa_{\Sigma}$  is the dust opacity. At the Hα wavelength,  $\kappa_{\Sigma} = 1.4701 \times 10^4 \text{ cm}^2 \text{ g}^{-1}$  for the LMC and  $\kappa_{\Sigma} = 1.2026 \times 10^4 \text{ cm}^2 \text{ g}^{-1}$  for the SMC (Weingartner & Draine 2001; Gordon et al. 2003) taking into account both absorption and scattering by dust grains.

Examining the  $\tau_{\text{dust}}$  map obtained reveals a mean  $\tau_{\text{dust}} = 1.08 \pm 0.04$  within  $5^\circ$  radius centred on  $(05^{\text{h}} 23^{\text{m}}, -69^\circ 45')$ <sub>J2000</sub> for the LMC. It is  $\tau_{\text{dust}} = 0.48 \pm 0.02$  within  $3^\circ$  radius centred on  $(00^{\text{h}} 52^{\text{m}}, -72^\circ 49')$ <sub>J2000</sub> in the SMC. In other words, the SMC's ISM is more transparent to the H $\alpha$  emission than the LMC, since it has a relatively lower dust mass surface density  $\Sigma_{\text{d}} < 0.1$  and metallicity (Jameson et al. 2016, and references there in).

### 3.2 Effective extinction

The dust optical depth obtained in Section 3.1 can be used to de-redden the observed H $\alpha$  emission if emitting sources (here ionized gas) are all behind a slab of dust with that optical depth ( $\tau_{\text{dust}}$ ). However, in reality, ionized gas and dust are mixed and hence only a fraction of  $\tau_{\text{dust}}$  must be considered. This fraction depends on the relative distributions of ionized gas and dust along the line of sight that is often unknown. Following Dickinson et al. (2003) and Tabatabaei et al. (2013a) we define an effective dust optical depth that should be considered to obtain the true extinction. It is given by multiplication of  $\tau_{\text{dust}}$  by the factor  $f_{\text{d}}$  that is the fraction of dust attenuating the H $\alpha$  emission along the line of sight:

$$\tau_{\text{eff}} \equiv f_{\text{d}} \times \tau_{\text{dust}} \quad (1)$$

with  $\tau_{\text{eff}}$  as the effective dust optical depth obtained at the H $\alpha$  wavelength. We note that  $\tau_{\text{eff}}$  in terms of visual extinction,  $A_{\text{V}}$ , is given by:

$$\tau_{\text{eff}} = \frac{A_{\text{V}} \kappa_{\text{H}\alpha}}{1.086 R_{\text{V}}} \quad (2)$$

with a total to selective ratio  $R_{\text{V}} = 3.41$  for the LMC and 2.74 for the SMC (Gordon et al. 2003). Dickinson et al. (2003) found that  $f_{\text{d}} = 0.33$  can best reproduce the Galactic plane's observed data, interpreting it as only one-third of dust along the line of sight is responsible for reddening. As the distribution of the ISM in dwarf systems can be different from normal-mass spiral galaxies, we expect that  $f_{\text{d}}$  also differs. Hence, we try to estimate  $f_{\text{d}}$  using observations of the Balmer decrements.

We use the H $\alpha$  and H $\beta$  emission data to measure the extinction using the following relations (e.g., Cardelli et al. 1989; Calzetti et al. 2000):

$$E(B - V)_{\text{Balmer}} = \frac{2.5}{\kappa(\text{H}\beta) - \kappa(\text{H}\alpha)} \log_{10} \left( \frac{F_{\text{H}\alpha}/F_{\text{H}\beta}}{2.86} \right) \quad (3)$$

$$A_{\text{V}} = R_{\text{V}} E(B - V)_{\text{Balmer}} \quad (4)$$

with  $E(B - V)$  the reddening and  $F_{\text{H}\alpha}$ ,  $F_{\text{H}\beta}$  the intrinsic H $\alpha$  and H $\beta$  fluxes. We adopted the theoretical  $F_{\text{H}\alpha}/F_{\text{H}\beta} = 2.86$  (Brookelhurst 1971; Osterbrock 1989).

Using the Calzetti et al. (2000) attenuation law, we obtain  $\kappa(\text{H}\alpha)$  and  $\kappa(\text{H}\beta)$  as 2.72 and 4.40 for the LMC and 2.19 and 3.76 for the SMC. Considering that  $A_{\text{V}}$  from equation (2) must be equal to that given by equation (4),  $f_{\text{d}}$  is obtained separately for H II regions and diffuse ISM as follows.

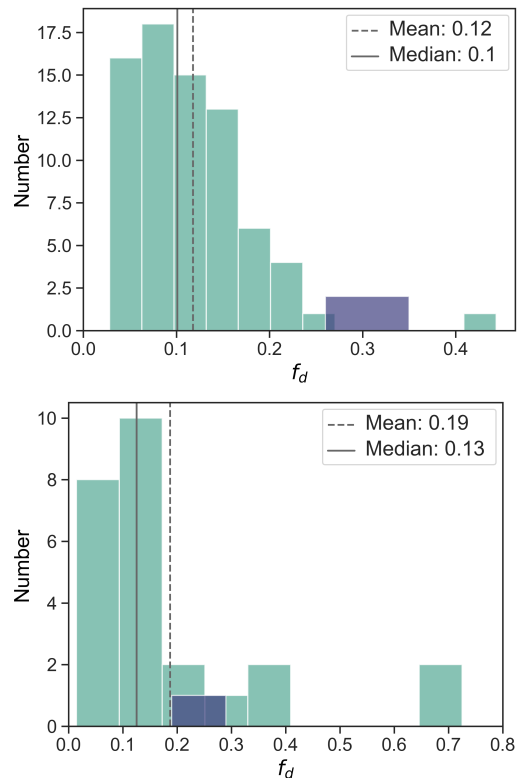


**Figure 2.** A histogram of  $f_{\text{d}}$  in H II regions (green) and diffuse regions (purple) for the LMC (top) and the SMC (bottom).

#### 3.2.1 Calibrating $f_{\text{d}}$ in H II regions

The  $F_{\text{H}\alpha}$  and  $F_{\text{H}\beta}$  fluxes were extracted from the Caplan catalog for a sample of 74 H II regions in the LMC and 25 H II regions in the SMC. We first derive their visual extinction  $A_{\text{V}}$  using equations (3) and (4). Extracting  $\tau_{\text{dust}}$  for the apertures in the Caplan catalog, we then calibrate and obtain  $f_{\text{d}}$  using equation (2). The  $A_{\text{V}}$  changes between 0.09 and 1.03 for the LMC with the median value of  $A_{\text{V}} = 0.35$ , which is larger by 34 per cent than in the SMC. Uncertainties in the observed fluxes affect  $A_{\text{V}}$  by less than 0.09 magnitudes in the LMC and 0.14 magnitudes in the SMC. The dust filling factor  $f_{\text{d}}$  obtained using equation (2) varies between 0.02 and 0.46 for the LMC and it changes between 0.01 and 0.72 for the SMC with a median value of  $f_{\text{d}} \simeq 0.1$  in both the LMC and the SMC H II regions (green bars in Fig. 2). Tables 4 and 5 list the resulting visual extinction  $A_{\text{V}}$ , dust mass surface density  $\Sigma_{\text{d}}$  and  $f_{\text{d}}$ .

Using the Caplan catalog we can only derive an average  $f_{\text{d}}$  in H II regions, but taking advantage of the MUSE observations we can map  $f_{\text{d}}$  in the two H II regions N44 and N180 (McLeod et al. 2018). We take  $32 \text{ \AA}$  wide (H $\alpha$  + N II) line based on MUSE observations covering a  $8' \times 8'$  area centred at  $(5^{\text{h}} 48^{\text{m}} 49.46^{\text{s}}, -70^\circ 03' 19.53'')$ <sub>J2000</sub> and  $(5^{\text{h}} 22^{\text{m}} 08.13^{\text{s}}, -67^\circ 56' 08.26'')$ <sub>J2000</sub> for N180 and N44, respectively. Details of spectral extraction are found in McLeod et al. (2018). We performed aperture photometry on the H $\alpha$  and H $\beta$  emission lines in N44 and N180 for each MUSE pixel resulting in a map of  $f_{\text{d}}$  (Fig. 3), indicating a good agreement with our integrated measurement within a  $4.89'$  diameter circular aperture of the Caplan catalog,  $f_{\text{d}} = 0.06$  and

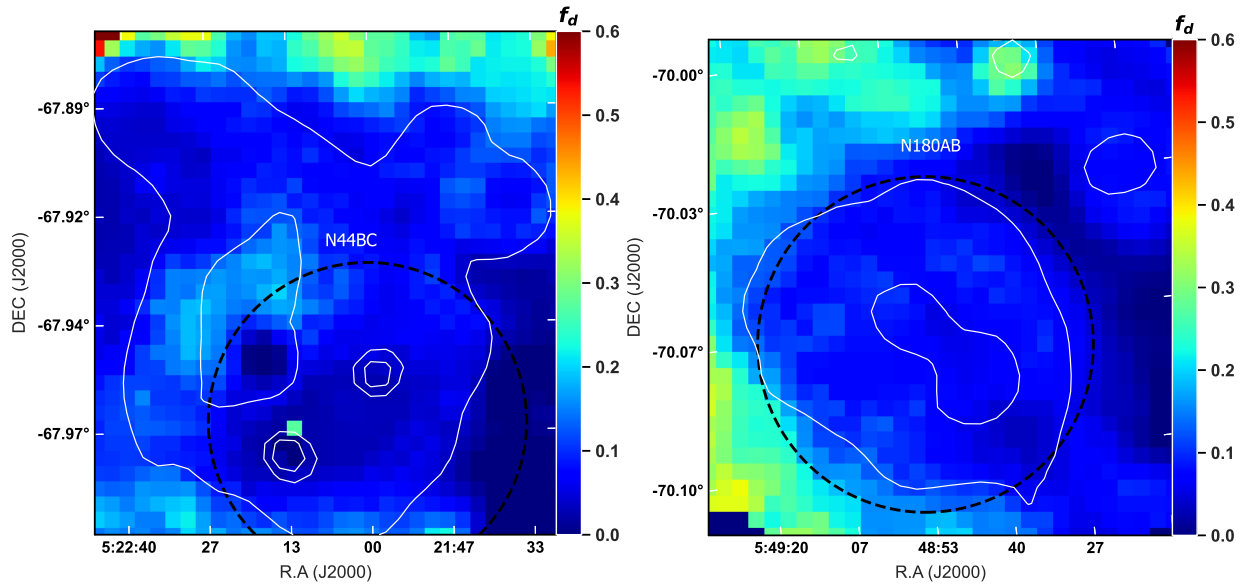


**Figure 3.** Map of the fraction of dust attenuating  $H\alpha$  emission  $f_d$  in the H II regions N44 (left) and N180 (right), overlaid with the  $H\alpha$  emission contours (white). Contours levels are  $1, 6,$  and  $8 \times 10^{-16} \text{ erg s}^{-1} \text{ cm}^{-2}$  (left) and  $1, 3,$  and  $6 \times 10^{-16} \text{ erg s}^{-1} \text{ cm}^{-2}$  (right). Black dashed circles are the apertures reported by [Caplan & Deharveng \(1985\)](#).

$f_d = 0.11$  in N44BC and N180AB. We note that the integrated  $H\alpha$  flux increases by about 20 per cent adopting the ( $H\alpha + N II$ ) bandwidth in comparison with the slab of narrow  $6\text{\AA}$   $H\alpha$  line. Inspecting the  $f_d$  maps, it is inferred that clumps of dust corresponding to dense regions of molecular gas have lower  $f_d$  than more diffuse regions (Fig. 4, top left).

### 3.2.2 Calibrating $f_d$ in the diffuse ISM

Determining  $f_d$  and  $\tau_{\text{eff}}$  should not be limited to only dense ionized gas in the H II regions because there is a considerable amount of  $H\alpha$  emission from lower density regions in the MCs. In this section, we use the MUSE observations of few SNRs (see Table 3) as they represent more diffuse regions than the H II regions. Using a Gaussian fit, we first derive the centre of each specific emission line (listed in Table 6), and then we obtain zero moments of the  $H\alpha$  line with a  $32\text{\AA}$  width and  $H\beta$  line using a  $6\text{\AA}$  width slab on each central line. The resulting  $f_d$  is higher in the SNRs by a factor of  $\sim 3$  compared to the H II regions, indicating that dust is better mixed with the ionized gas in the SNRs than in the H II regions (purple bars in Fig. 2). In other words, as dust is clumpier in the H II regions than in the SNRs, the dust filling factor is smaller in the H II regions. Table 6 shows the resulting visual extinction  $A_V$ , dust mass surface density  $\Sigma_d$ , and  $f_d$  for the MUSE/VLT fields.

Maps of  $f_d$  could only be derived for a few H II regions and SNRs using MUSE observations. To map the variation of  $f_d$  for the entire galaxy, its correlation with the total neutral gas is first investigated for the given fields and sources (Fig. 4, top left). Then a calibration relation is built to map  $f_d$  over the entire galaxy. We measured the total gas surface density as  $\Sigma_{\text{gas}} = \Sigma_{\text{H I}} + \Sigma_{\text{H mol}}$  where  $\Sigma_{\text{H mol}} = 2N(H_2) = 2X_{\text{CO}} \times I_{\text{CO}}$  and adopting a conversion factor  $X_{\text{CO}} = 2 \times 10^{20} \text{ cm}^{-2} (\text{K km s}^{-1})^{-1}$  ([Strong & Mattox 1996](#)). The similar conversion factor  $X_{\text{CO}} \approx 2.76 \times 10^{20} \text{ cm}^{-2} (\text{K km s}^{-1})^{-1}$  was re-

ported for the LMC ([Leroy et al. 2011](#)). Excluding pixels weaker than  $3\sigma$  RMS ( $\sigma = 3.3 \times 10^{19} \text{ H cm}^{-2}$ ) in total gas surface density, we found a relation between  $f_d$  and  $\Sigma_{\text{gas}}$  in the LMC:

$$\text{Log } f_d (\text{LMC}) = (-0.62 \pm 0.04) \text{Log } \Sigma_{\text{gas}} - (0.67 \pm 0.03) \quad (5)$$

We then construct a synthesized map for  $f_d$  using equation (5) in the LMC (Fig. 4, top right). In the H II regions, the median value of  $f_d$  is about 0.1 that agrees with the more direct estimate outlined in Section 3.2.1 with a mean  $\Sigma_{\text{gas}} = 3 \times 10^{21} \text{ H cm}^{-2}$ . This factor is higher in regions of lower density gas ( $\Sigma_{\text{gas}} < 8 \times 10^{20} \text{ H cm}^{-2}$ ) as expected. We found a mean value  $f_d = 0.29 \pm 0.04$  in the LMC within  $5^\circ$  of the central point ( $05^{\text{h}} 23^{\text{m}} 34^{\text{s}}, -69^\circ 45' 22''$ )<sub>J2000</sub>, which is in a good agreement with Galactic value ([Dickinson et al. 2003](#)). However, we should note that we found a variation of 0.2–0.3 in different ISM gas regimes.

We note that no correlation is found between  $f_d$  and neutral gas in the SMC, and hence no calibration relation can be extracted, perhaps due to the lack of a deep and full-coverage CO map. Thus, we take the median value of  $f_d = 0.1$  to map the extinction in the SMC. In diffuse regions where it is expected to have deviations from  $f_d = 0.1$ , changing  $f_d$  from 0.1 to 0.3 affects (increases) the intrinsic  $H\alpha$  and hence the thermal fraction by less than 22 per cent as in these regions  $\tau_{\text{eff}} < 1$ .

### 3.2.3 Extinction maps and de-reddening the $H\alpha$ emission

Fig. 4 (bottom row) shows the final maps of the effective extinction  $\tau_{\text{eff}}$ . In the LMC, we find on the average  $\tau_{\text{eff}} = 0.08 \pm 0.01$  compared to  $\tau_{\text{eff}} = 0.05 \pm 0.02$  in the SMC. Maximum extinction occurs in the centre of 30 Dor with  $\tau_{\text{eff}} = 0.75 \pm 0.11$ . We use the extinction map to de-

**Table 4.** Dust surface density ( $\Sigma_d$ ), visual extinction ( $A_V$ ), the fraction of dust attenuating H $\alpha$  emission ( $f_d$ ), and thermal fractions at 0.166 GHz ( $f_{\text{th}}^{0.166 \text{ GHz}}$ ) and 1.4 GHz ( $f_{\text{th}}^{1.4 \text{ GHz}}$ ) obtained for H II regions in the LMC. The Balmer-line-decrement ratio ( $F_{\text{H}\alpha}/F_{\text{H}\beta}$ ), and the size of the sources are taken from [Caplan & Deharveng \(1985\)](#).

Source	R.A (J2000) (deg)	Dec (J2000) (deg)	Radius (arcmin)	$F_{\text{H}\alpha}/F_{\text{H}\beta}$	$\Sigma_d$ ( $10^{-5} \text{ g cm}^{-2}$ )	$A_V$	$f_d$	$f_{\text{th}}^{0.166 \text{ GHz}}$ (%)	$f_{\text{th}}^{1.4 \text{ GHz}}$ (%)
N77E	72.444	-69.199	4.89	3.52	$16.73 \pm 0.69$	0.46	$0.14 \pm 0.03$	$20.4 \pm 3.5$	$80.2 \pm 10.1$
N4AB	72.977	-66.907	4.89	3.24	$19.62 \pm 0.61$	0.28	$0.07 \pm 0.02$	$46.1 \pm 8.7$	$69.6 \pm 9$
N79AB	72.931	-69.398	4.89	3.78	$17.63 \pm 0.52$	0.61	$0.17 \pm 0.03$	$28.2 \pm 4.2$	$64.3 \pm 8.1$
N79DE	73.061	-69.345	4.89	3.50	$22.91 \pm 0.49$	0.45	$0.10 \pm 0.02$	$36.3 \pm 5.5$	$94.8 \pm 12.1$
N81	73.195	-69.224	4.89	3.65	$14.72 \pm 0.66$	0.54	$0.18 \pm 0.03$	-	$127.7 \pm 16.8$
N83A	73.494	-69.200	4.89	3.77	$24.77 \pm 0.79$	0.61	$0.12 \pm 0.02$	$55.8 \pm 8.4$	$79.3 \pm 10.2$
N83north	73.596	-69.154	2.00	3.68	$19.24 \pm 0.55$	0.56	$0.14 \pm 0.02$	$98.2 \pm 16$	$83.8 \pm 10.6$
N11F	74.164	-66.522	4.89	3.17	$18.99 \pm 0.53$	0.23	$0.06 \pm 0.02$	$126.9 \pm 20.4$	$117.1 \pm 15$
N11B	74.201	-66.404	4.89	3.36	$30.22 \pm 0.89$	0.35	$0.06 \pm 0.01$	$137.2 \pm 20.3$	$101 \pm 13.2$
N91	74.291	-68.415	4.89	3.42	$14.70 \pm 0.53$	0.39	$0.13 \pm 0.03$	$17.1 \pm 2.7$	$111.1 \pm 14.1$
N11CD	74.428	-66.461	4.89	3.21	$28.33 \pm 0.77$	0.25	$0.04 \pm 0.02$	$130.5 \pm 19.3$	$103.8 \pm 13.4$
N11E	74.535	-66.362	4.89	3.36	$22.68 \pm 0.55$	0.35	$0.08 \pm 0.02$	$87.4 \pm 14.9$	$82.8 \pm 10.5$
N23A	76.222	-68.056	4.89	3.28	$8.56 \pm 0.42$	0.30	$0.18 \pm 0.05$	-	$89.6 \pm 11.1$
N103B	77.178	-68.764	4.89	3.24	$9.92 \pm 0.49$	0.28	$0.14 \pm 0.04$	$11.4 \pm 1.6$	$44.5 \pm 5.5$
N103A	77.344	-68.768	2.00	3.17	$11.06 \pm 0.68$	0.23	$0.10 \pm 0.04$	-	$48.4 \pm 6.1$
N105A	77.477	-68.891	4.89	3.28	$28.19 \pm 0.78$	0.30	$0.05 \pm 0.02$	$77.6 \pm 11.2$	$74.9 \pm 9.6$
N113south	78.340	-69.365	4.89	3.16	$24.44 \pm 0.58$	0.22	$0.04 \pm 0.02$	$56.8 \pm 8.2$	$90.4 \pm 11.3$
N113north	78.397	-69.301	4.89	3.27	$10.89 \pm 0.50$	0.29	$0.14 \pm 0.04$	$65.2 \pm 9.5$	$92.2 \pm 11.4$
N119	79.663	-69.236	4.89	3.04	$13.93 \pm 0.34$	0.13	$0.05 \pm 0.03$	$100.5 \pm 14.5$	$118.9 \pm 15$
N120(SNR)	79.643	-69.648	2.00	2.98	$11.68 \pm 0.37$	0.09	$0.04 \pm 0.04$	-	$54.2 \pm 6.7$
N120AB	79.751	-69.637	2.00	3.06	$26.49 \pm 0.31$	0.15	$0.03 \pm 0.02$	-	$71.3 \pm 8.8$
N120ABC	79.817	-69.653	4.89	3.14	$17.48 \pm 0.48$	0.21	$0.06 \pm 0.03$	$40.6 \pm 5.7$	$75.6 \pm 9.3$
N44BC	80.503	-67.970	4.89	3.33	$33.73 \pm 0.73$	0.34	$0.05 \pm 0.01$	$62.6 \pm 8.9$	$70.5 \pm 8.9$
N44I	80.609	-67.896	4.89	3.14	$21.40 \pm 0.56$	0.21	$0.05 \pm 0.02$	$42.9 \pm 6.1$	$59 \pm 7.5$
N44D	80.686	-68.076	4.89	3.44	$32.21 \pm 0.79$	0.41	$0.06 \pm 0.01$	-	$65.9 \pm 8.3$
N138A	81.238	-68.480	4.89	3.44	$19.78 \pm 0.60$	0.41	$0.10 \pm 0.02$	-	$69.7 \pm 8.8$
N48B	81.396	-66.304	4.89	3.64	$16.24 \pm 0.67$	0.53	$0.16 \pm 0.03$	$8.5 \pm 1.2$	$20.3 \pm 2.5$
N51D	81.508	-67.499	4.89	2.99	$5.22 \pm 0.39$	0.10	$0.09 \pm 0.09$	$93.3 \pm 13.8$	$104.8 \pm 12.8$
N51E	81.600	-67.622	4.89	3.31	$6.65 \pm 0.50$	0.32	$0.24 \pm 0.07$	$26.5 \pm 4.2$	$88.8 \pm 10.9$
N143	81.598	-69.315	4.89	3.14	$4.86 \pm 0.35$	0.21	$0.21 \pm 0.09$	$13.6 \pm 2.1$	$83.8 \pm 10.5$
N144AB	81.637	-68.825	4.89	3.47	$17.67 \pm 0.56$	0.43	$0.12 \pm 0.03$	$114 \pm 16.9$	$128.3 \pm 16.6$
N144	81.635	-68.863	4.89	3.46	$9.43 \pm 0.50$	0.42	$0.22 \pm 0.05$	$94.2 \pm 14.1$	$123 \pm 15.6$
N144	81.745	-68.825	4.89	3.45	$9.97 \pm 0.51$	0.41	$0.21 \pm 0.05$	$102.9 \pm 15.3$	$130 \pm 16.6$
N51C	81.901	-67.455	4.89	3.11	$12.37 \pm 0.54$	0.18	$0.07 \pm 0.04$	$85.4 \pm 12.8$	$110.8 \pm 13.8$
N51A	82.002	-67.424	4.89	3.21	$16.21 \pm 0.52$	0.25	$0.08 \pm 0.03$	$49.7 \pm 7.4$	$104.6 \pm 13.2$
N206	82.400	-71.001	4.89	3.51	$5.10 \pm 0.30$	0.45	$0.44 \pm 0.09$	-	$87.9 \pm 10.9$
N206	82.587	-71.101	4.89	3.46	$17.00 \pm 0.60$	0.42	$0.12 \pm 0.03$	$68.9 \pm 10.3$	$81.7 \pm 10.3$
N206A	82.805	-71.069	4.89	3.46	$21.29 \pm 0.59$	0.42	$0.10 \pm 0.02$	$81.5 \pm 11.7$	$83.5 \pm 10.5$
N148	82.937	-68.532	4.89	3.34	$25.23 \pm 0.63$	0.34	$0.07 \pm 0.02$	-	$78.5 \pm 10.2$
N55north	83.024	-66.411	4.89	3.23	$16.02 \pm 0.53$	0.27	$0.08 \pm 0.03$	$119.4 \pm 22.7$	$128.4 \pm 16.8$
N55A	83.118	-66.467	4.89	3.21	$14.59 \pm 0.41$	0.25	$0.09 \pm 0.03$	$147.6 \pm 25.7$	$133.5 \pm 17.3$
N57A	83.099	-67.694	4.89	3.41	$31.55 \pm 0.58$	0.39	$0.06 \pm 0.01$	$65.2 \pm 9.8$	$124.4 \pm 16.4$
N57C	83.290	-67.713	4.89	3.42	$18.64 \pm 0.48$	0.39	$0.11 \pm 0.02$	-	$88.6 \pm 11.4$
Filaments	83.353	-67.453	4.89	3.00	$11.08 \pm 0.49$	0.10	$0.05 \pm 0.04$	$37.4 \pm 5.6$	$69.7 \pm 8.7$

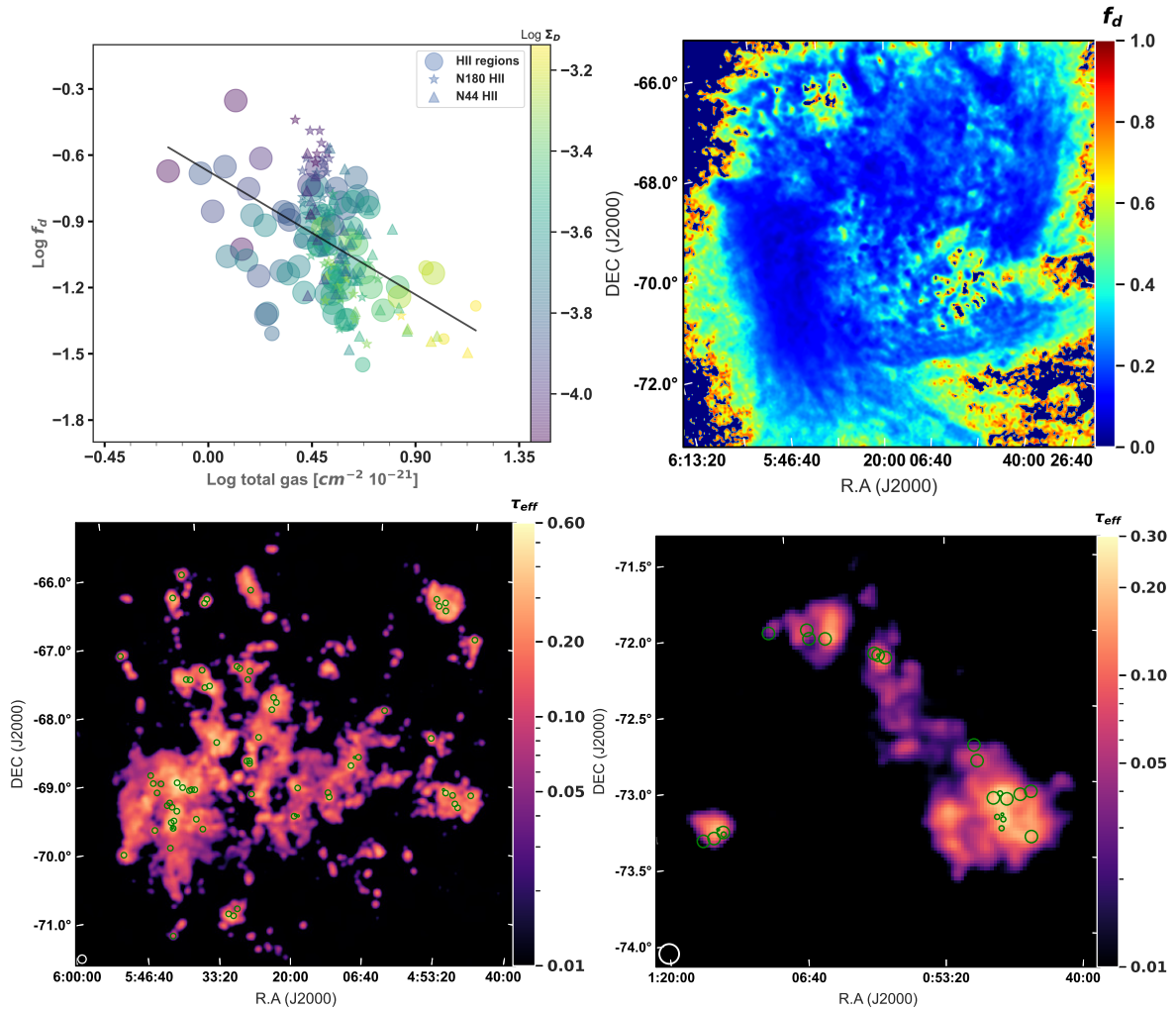


**Figure 4.** Top: the fraction of dust attenuating  $H\alpha$  emission  $f_d$  vs the total gas density  $\Sigma_{\text{gas}}$  (left) in separate fields and the map of  $f_d$  (right) in the LMC. Solid line shows the Ordinary Least Squares (OLS) bisector fit in log-log space used as an independent calibration of  $f_d$ . Bottom: effective dust optical depth ( $\tau_{\text{eff}}$ ) at  $H\alpha$  wavelength for the LMC (left) and the SMC (right) shown in log scale. Green circles indicate the position of  $H\text{ II}$  regions inside the MCs. The beam sizes of  $221''$  (for the LMC) and  $235''$  (for the SMC) are shown in the lower left corner of the maps.

redden the  $H\alpha$  map and obtain the intrinsic  $H\alpha$  intensity  $I_0$  using  $I = I_0 e^{-\tau_{\text{eff}}}$ .

Adopting the extinction map  $\tau_{\text{eff}}$  to de-redden  $H\alpha$  yields  $\simeq 20$  per cent obscuration for the LMC. This is higher than that in the SMC ( $\simeq 4$  per cent) and similar to the correction factor for the dust obscuration reported for M33 ( $\simeq 13$  per cent, Tabatabaei et al. 2007). Integration of the dust corrected  $H\alpha$  map out to a radius of  $5^\circ$  yields an intrinsic  $H\alpha$  luminosity  $L_{H\alpha} = (3.67 \pm 0.47) \times 10^{40} \text{ erg s}^{-1}$  for the LMC. The SMC has a luminosity of  $L_{H\alpha} = (6.87 \pm 1.06) \times 10^{39} \text{ erg s}^{-1}$  out to a radius of  $3.5^\circ$ .

#### 4 Separation of Thermal and Non-thermal Radio Emission

Separating the thermal and non-thermal radio emission is critical to study cosmic-ray energy loss mechanisms and the total magnetic fields. A pure non-thermal synchrotron spectral index map can be obtained using the TRT method, in which the thermal (free-free) emission is obtained using the

de-reddened  $H\alpha$  emission as its template (Tabatabaei et al. 2013a).

#### 4.1 From $H\alpha$ emission to radio free-free emission

The  $H\alpha$  intensity is related to the emission measure (EM) depending on the transparency of the ISM to Lyman continuum photons. In case of ( $\tau_{Ly\alpha} \gg 1$ ) condition  $\dagger$  which is usually denoted as Case B recombination (Osterbrock 1989),  $I_{H\alpha}$  in  $\text{erg cm}^{-2} \text{ s}^{-1} \text{ sr}^{-1}$  units is given by (Valls-Gabaud 1998):

$$I_{H\alpha} = 9.41 \times 10^{-8} T_e^{-1.017} 10^{(-\frac{0.029}{T_e})} EM \quad (6)$$

where  $T_e$  is the electron temperature in units of  $10^4 \text{ K}$ , and  $EM$  in  $\text{cm}^{-6} \text{ pc}$ . Equation (6) is more than 1 per cent precise for the electron temperatures of 5,000 to 20,000 K. Oster

$\dagger$  Optically thin condition is discussed in Section 6.5.

Table 4. Continued.

Source	R.A (J2000) (deg)	Dec (J2000) (deg)	Radius (arcmin)	$F_{H\alpha}/F_{H\beta}$	$\Sigma_d$ ( $10^{-5} \text{ g cm}^{-2}$ )	$A_V$	$f_d$	$f_{\text{th}}^{0.166 \text{ GHz}}$ (%)	$f_{\text{th}}^{1.4 \text{ GHz}}$ (%)
N154south	83.725	-69.798	4.89	3.20	$9.70 \pm 0.48$	0.25	$0.13 \pm 0.05$	$37 \pm 5.2$	$66.7 \pm 8.2$
N63A	83.892	-66.031	4.89	3.19	$8.61 \pm 0.44$	0.24	$0.14 \pm 0.05$	-	$18.5 \pm 2.3$
N59A	83.840	-67.585	4.89	3.84	$24.33 \pm 0.50$	0.65	$0.13 \pm 0.02$	$97.9 \pm 14.2$	$75.5 \pm 9.7$
N59B	83.986	-67.577	4.89	3.48	$21.81 \pm 0.59$	0.43	$0.10 \pm 0.02$	$66.8 \pm 9.7$	$75.6 \pm 9.7$
N157	83.952	-69.210	4.89	3.83	$32.62 \pm 0.78$	0.64	$0.10 \pm 0.01$	$29.2 \pm 4.2$	$52.5 \pm 6.8$
N157	84.086	-69.205	4.89	3.70	$18.51 \pm 0.45$	0.57	$0.15 \pm 0.02$	$29.3 \pm 4.1$	$54.2 \pm 6.9$
N154A	83.973	-69.646	4.89	3.35	$23.51 \pm 0.68$	0.35	$0.07 \pm 0.02$	$62.6 \pm 8.9$	$86.6 \pm 11$
N157	84.177	-69.216	4.89	3.69	$23.89 \pm 0.73$	0.56	$0.12 \pm 0.02$	$31.9 \pm 4.5$	$58.3 \pm 7.4$
N64AB	84.274	-66.361	4.89	3.23	$18.44 \pm 0.58$	0.27	$0.07 \pm 0.02$	$64.6 \pm 11.5$	$112.6 \pm 14.6$
N157B	84.449	-69.165	4.89	4.22	$41.44 \pm 0.72$	0.86	$0.10 \pm 0.01$	$43.1 \pm 6.8$	$47.6 \pm 6.6$
N157A-30dor	84.660	-69.088	4.89	4.57	$44.22 \pm 3.32$	1.03	$0.12 \pm 0.01$	$110.4 \pm 21.9$	$65.6 \pm 9.8$
N158C	84.769	-69.506	4.89	3.62	$35.33 \pm 0.39$	0.52	$0.07 \pm 0.01$	$73.2 \pm 10.7$	$87 \pm 11.4$
N159A	84.908	-69.771	1.06	4.01	$71.59 \pm 1.08$	0.74	$0.05 \pm 0.01$	$47.2 \pm 6.6$	$37.7 \pm 4.8$
N16OAD	84.926	-69.646	4.89	3.73	$51.23 \pm 0.95$	0.58	$0.06 \pm 0.01$	$6.6 \pm 1$	$65.4 \pm 8.7$
N158	84.955	-69.441	4.89	3.34	$17.32 \pm 0.40$	0.34	$0.10 \pm 0.03$	$43.4 \pm 6.1$	$70.2 \pm 8.8$
N159	84.988	-69.752	4.89	4.09	$53.88 \pm 1.05$	0.79	$0.07 \pm 0.01$	$28.9 \pm 4.1$	$42.5 \pm 5.5$
N159BD	84.989	-69.733	2.00	4.24	$56.16 \pm 1.25$	0.87	$0.08 \pm 0.01$	-	$46.5 \pm 6.1$
N159C	85.025	-69.756	1.06	3.59	$68.06 \pm 0.14$	0.50	$0.04 \pm 0.01$	$50.3 \pm 7.2$	$41.4 \pm 5.4$
N158A	85.040	-69.376	4.89	3.30	$7.19 \pm 0.45$	0.32	$0.22 \pm 0.06$	$17.8 \pm 2.4$	$36.2 \pm 4.4$
N16OBCE	85.046	-69.667	4.89	3.47	$33.74 \pm 0.54$	0.43	$0.06 \pm 0.01$	-	$89.7 \pm 11.7$
N158	85.151	-69.412	4.89	3.25	$7.68 \pm 0.41$	0.28	$0.18 \pm 0.06$	$21.3 \pm 2.9$	$41.6 \pm 5$
N175	85.180	-70.041	4.89	3.52	$11.55 \pm 0.45$	0.46	$0.20 \pm 0.04$	$12.4 \pm 1.8$	$28.8 \pm 3.6$
Filaments	85.331	-69.084	4.89	3.37	$10.20 \pm 0.57$	0.36	$0.18 \pm 0.04$	$20.5 \pm 2.8$	$48.8 \pm 6$
N214C	85.410	-71.337	4.89	3.29	$10.72 \pm 0.43$	0.31	$0.14 \pm 0.04$	$10.2 \pm 1.5$	$75.3 \pm 9.1$
NGC2100	85.526	-69.211	4.89	3.19	$9.96 \pm 0.64$	0.24	$0.12 \pm 0.04$	$17.5 \pm 2.4$	$47.5 \pm 5.8$
N164	85.648	-69.068	4.89	3.83	$20.90 \pm 0.38$	0.64	$0.15 \pm 0.02$	$37.1 \pm 5.2$	$62.7 \pm 7.8$
N165	85.723	-68.947	4.89	3.43	$12.88 \pm 0.55$	0.40	$0.16 \pm 0.04$	-	$37.1 \pm 4.6$
N163	85.770	-69.759	4.89	3.89	$23.30 \pm 0.45$	0.68	$0.15 \pm 0.02$	$10.2 \pm 1.4$	$49 \pm 6.1$
N74A	86.427	-67.149	4.89	3.04	$9.44 \pm 0.53$	0.13	$0.07 \pm 0.05$	-	$126.8 \pm 23$
N180AB	87.215	-70.071	4.89	3.30	$23.07 \pm 0.56$	0.32	$0.07 \pm 0.02$	$63.9 \pm 9.3$	$106.1 \pm 13.4$

(1961) presents an expression of the free-free continuum optical thickness radiated from an ionized gas:

$$\tau_c = 0.08235 \times a T_e^{-1.35} \nu_{\text{GHz}}^{-2.1} (1 + 0.08) EM \quad (7)$$

with  $a \simeq 1$  and the continuum optical depth is corrected for singly ionized He atoms by the factor  $(1+0.08)$ .

The brightness temperature  $T_b$  of the radio continuum (free-free) emission in units of Kelvin is given by:

$$T_b = T_e(1 - e^{-\tau_c}) \quad (8)$$

The brightness temperature is converted to the radio flux density ( $\text{Jy beam}^{-1}$ ) using a factor of 1.0, 78.2, and 919.3 for the LMC at 0.166 GHz, 1.4 GHz and 4.8 GHz respectively. These factors are 1.2 and 88.4 for the SMC at 0.166 GHz and 1.4 GHz respectively. The electron temperature is the only free parameter in this conversion. Different methods of electron temperature determination (Dufour 1975; Dufour &

Harlow 1977; Vermeij & van der Hulst 2002; Peck et al. 1997) indicate that  $8000 \text{ K} < T_e < 12000 \text{ K}$  in the MCs. However, we adopt  $T_e = 10^4 \text{ K}$  as this variation would not change the thermal emission by more than 20 per cent.

The free-free maps are presented in Figs. 5, 6 (left panels) at frequencies of 0.166, 1.4, and 4.8 GHz. The strongest thermal emission is visible in the MCs' H II regions, in particular, the LMC H II region 30 Dor has a significant amount of free-free emission reaching  $6 \text{ Jy beam}^{-1}$  at 0.166 GHz. The other LMC H II regions like N11 and N44 reach  $0.5 \text{ Jy beam}^{-1}$  as well as N66 in the SMC.

## 4.2 Mapping synchrotron emission

The synchrotron emission maps are obtained at frequencies of 0.166, 1.4, and 4.8 GHz by subtracting the thermal map from the observed RC map (Fig. 5 and 6). Strong synchrotron emission emerges from the brightest H II complex of the LMC, 30 Dor, possibly due to strong magnetic field and/or ener-

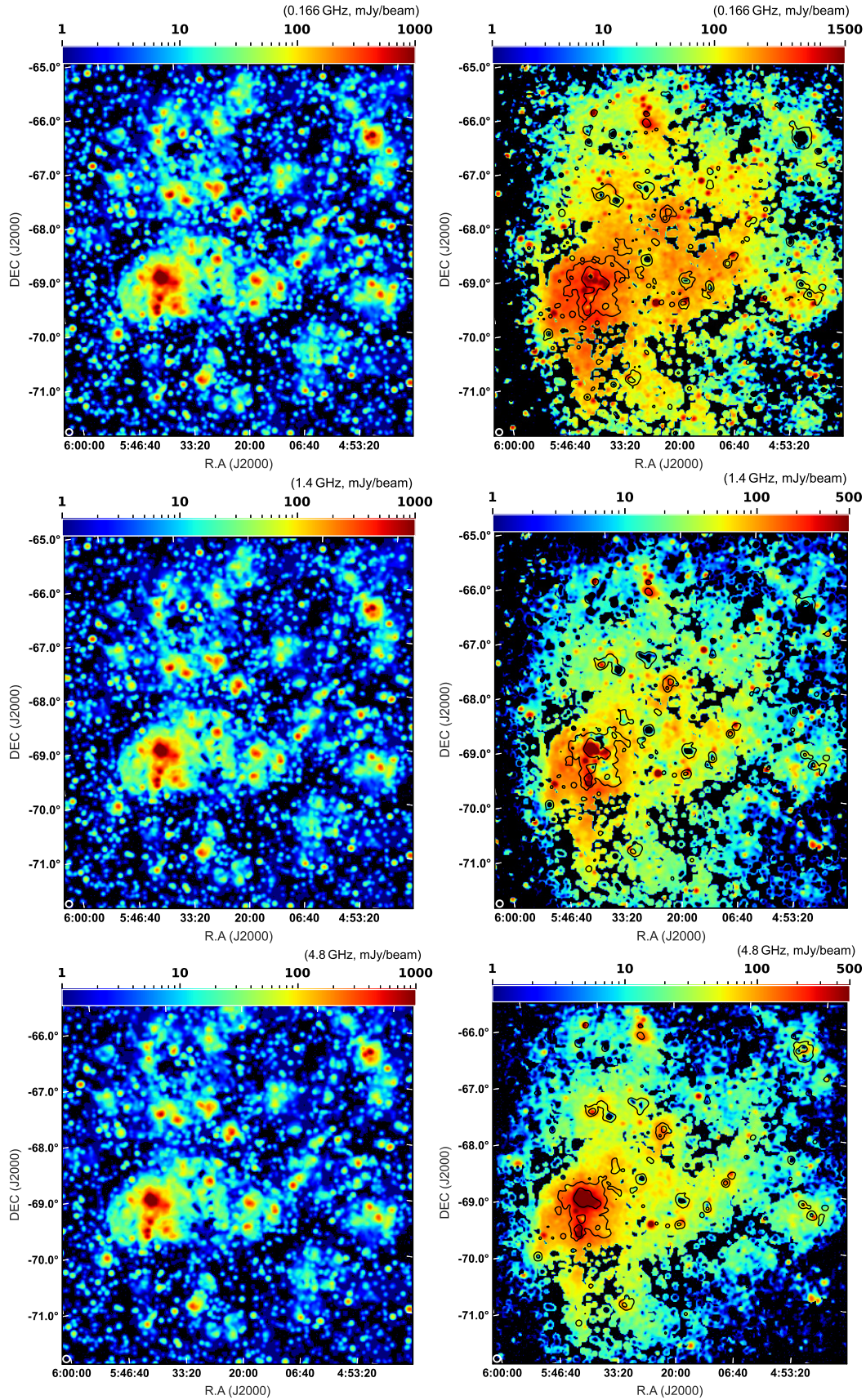


**Figure 5.** The LMC– The thermal free-free (left) and the non-thermal synchrotron (right) emission maps at 0.166 GHz (top), 1.4 GHz (middle) and 4.8 GHz (bottom). Colour bars show the intensities in units of  $\text{mJy beam}^{-1}$  in log scale. The non-thermal maps are overlaid with contours of the thermal emission with levels of 40 and  $100 \text{ mJy beam}^{-1}$ . The beam size of  $221''$  is shown in the lower left corner of the maps.

**Table 5.** Dust surface density ( $\Sigma_d$ ), visual extinction ( $A_V$ ), the fraction of dust attenuating H $\alpha$  emission ( $f_d$ ), and thermal fractions at 0.166 GHz ( $f_{\text{th}}^{0.166 \text{ GHz}}$ ) and 1.4 GHz ( $f_{\text{th}}^{1.4 \text{ GHz}}$ ) obtained for H II regions in the SMC. The Balmer-line-decrement ratio ( $F_{\text{H}\alpha}/F_{\text{H}\beta}$ ), and the size of the sources are taken from [Caplan & Deharveng \(1985\)](#).

Source	R.A (J2000) (deg)	Dec (J2000) (deg)	Radius (arcmin)	$F_{\text{H}\alpha}/F_{\text{H}\beta}$	$\Sigma_d$ ( $10^{-5} \text{ g cm}^{-2}$ )	$A_V$	$f_d$	$f_{\text{th}}^{0.166 \text{ GHz}}$ (%)	$f_{\text{th}}^{1.4 \text{ GHz}}$ (%)
N13AB	11.347	-73.380	4.89	3.51	$15.60 \pm 0.30$	0.39	$0.15 \pm 0.05$	$27.5 \pm 5.8$	$59.3 \pm 6.3$
N12Ba	11.387	-73.080	4.89	3.42	$5.63 \pm 0.48$	0.34	$0.37 \pm 0.15$	$39.1 \pm 8.2$	$87.6 \pm 10.1$
N12-Ab	11.629	-73.101	4.89	3.34	$11.86 \pm 0.39$	0.29	$0.15 \pm 0.07$	-	$71.5 \pm 7.4$
N19	11.932	-73.134	4.89	3.46	$15.37 \pm 0.14$	0.36	$0.14 \pm 0.05$	-	$56.1 \pm 5.3$
N22	12.004	-73.270	2.00	3.46	$24.31 \pm 0.17$	0.36	$0.09 \pm 0.03$	$53 \pm 9.6$	$75.4 \pm 7.1$
N25-N26	12.029	-73.237	1.06	3.78	$31.18 \pm 0.44$	0.53	$0.10 \pm 0.03$	$51.5 \pm 9.6$	$79.8 \pm 7.6$
N24	12.040	-73.329	2.00	3.15	$15.57 \pm 0.27$	0.18	$0.07 \pm 0.05$	-	$51 \pm 5.1$
N27	12.088	-73.099	2.00	3.43	$37.23 \pm 0.36$	0.34	$0.06 \pm 0.02$	-	$84.7 \pm 7.8$
N28	12.148	-73.254	2.00	3.29	$10.18 \pm 0.20$	0.26	$0.16 \pm 0.08$	$40.3 \pm 7.3$	$72.6 \pm 7.2$
N30	12.240	-73.129	4.89	3.45	$17.92 \pm 0.07$	0.35	$0.12 \pm 0.04$	$31.4 \pm 5.6$	$79.7 \pm 7.7$
N36cg	12.616	-72.884	4.89	3.16	$6.26 \pm 0.45$	0.19	$0.18 \pm 0.13$	$44.5 \pm 8.3$	$92.7 \pm 10$
N37dg	12.687	-72.780	4.89	3.40	$2.88 \pm 0.28$	0.33	$0.69 \pm 0.29$	$23.6 \pm 4.4$	$81.5 \pm 9.2$
N66i	14.619	-72.195	4.89	3.08	$9.97 \pm 0.22$	0.14	$0.09 \pm 0.08$	-	$91.6 \pm 9.5$
N66ii	14.771	-72.178	4.89	3.08	$11.84 \pm 0.28$	0.14	$0.07 \pm 0.07$	$20.5 \pm 3.5$	$78.2 \pm 8$
N66iii	14.771	-72.178	1.06	2.93	$19.13 \pm 0.07$	0.05	$0.01 \pm 0.04$	-	$76.6 \pm 7.7$
N66iv	14.858	-72.165	4.89	3.13	$8.09 \pm 0.30$	0.17	$0.13 \pm 0.10$	$32.7 \pm 5.6$	$68.2 \pm 7.1$
N76	15.902	-72.057	4.89	3.04	$12.01 \pm 0.27$	0.12	$0.06 \pm 0.07$	$29.5 \pm 5.2$	$65.3 \pm 6.6$
N78ii	16.285	-71.993	4.89	3.35	$6.10 \pm 0.47$	0.30	$0.30 \pm 0.13$	-	$66.1 \pm 7.2$
N80	17.106	-71.999	4.89	2.96	$3.42 \pm 0.45$	0.07	$0.12 \pm 0.24$	$30.3 \pm 7$	$79.8 \pm 9.7$
N81	17.284	-73.202	4.89	2.97	$1.07 \pm 0.13$	0.07	$0.41 \pm 0.76$	-	$129.8 \pm 24.6$
N83A	18.451	-73.301	2.00	3.04	$13.29 \pm 0.26$	0.12	$0.05 \pm 0.06$	-	$115.4 \pm 11.9$
N83	18.456	-73.288	4.89	3.28	$13.07 \pm 0.38$	0.26	$0.12 \pm 0.06$	-	$111.8 \pm 11.7$
N84C	18.567	-73.266	1.06	3.91	$20.59 \pm 0.43$	0.59	$0.18 \pm 0.04$	-	$105.4 \pm 10.4$
N84AB	18.681	-73.322	4.89	3.19	$11.26 \pm 0.36$	0.21	$0.11 \pm 0.07$	-	$117.7 \pm 12.8$
N85fg	18.931	-73.334	4.89	3.17	$1.65 \pm 0.30$	0.25	$0.72 \pm 0.51$	-	$84 \pm 11.2$

**Table 6.** Measured fluxes  $F_{\text{H}\alpha}$  and  $F_{\text{H}\beta}$  of the MUSE SNR fields and their corresponding central wavelengths (CW). Also shown are dust surface density ( $\Sigma_d$ ), visual extinction ( $A_V$ ), and fraction of dust attenuating H $\alpha$  emission ( $f_d$ ).

Field	CW $_{\text{H}\alpha}$ ( $\text{\AA}$ )	CW $_{\text{H}\beta}$ ( $\text{\AA}$ )	$F_{\text{H}\alpha}$ ( $10^{-12} \text{ erg s}^{-1} \text{ cm}^{-2}$ )	$F_{\text{H}\beta}$ ( $10^{-12} \text{ erg s}^{-1} \text{ cm}^{-2}$ )	$\Sigma_d$ ( $10^{-5} \text{ g cm}^{-2}$ )	$A_V$	$f_d$
LMC/N49	6567.48	4864.98	$50.9 \pm 2.5$	$11.9 \pm 0.6$	$16.6 \pm 1.2$	$0.9 \pm 0.5$	$0.3 \pm 0.1$
LMC/SNR 0540-69.3	6568.74	4866.24	$4.4 \pm 0.2$	$0.9 \pm 0.1$	$16.8 \pm 0.1$	$1.2 \pm 0.5$	$0.3 \pm 0.1$
SMC/1E0102-7219	6566.07	4863.57	$3.3 \pm 0.1$	$1.1 \pm 0.1$	$6.0 \pm 0.5$	$0.2 \pm 0.1$	$0.2 \pm 0.1$

getic CREs in this massive star-forming region. This source is the most prominent feature of the synchrotron emission from 0.166 GHz to 4.8 GHz. Extended diffuse synchrotron emission is also clearly visible around 30 Dor. At 1.4 GHz, this region is affected by observational artefacts ([Hughes et al. 2007](#)) reducing the sensitivity to detect the diffuse emission at distances about 0.6 kpc from the centre of 30 Dor in the north. In the SMC, an extended synchrotron emission is found along its bar. The synchrotron emission is also strong in other H II regions, which are classically considered as thermal sources such as H II N44 and N11 of the LMC, N66 and N19 in the SMC as indicated by contours of the thermal emission over-

laid on the non-thermal maps in Figs. 5, 6. This non-thermal intensity is probably due to SNRs and strong non-thermal shocks in these young, massive star clusters and associations. Similar non-thermal emission was previously shown to exist in the H II regions of M33 ([Tabatabaei et al. 2007](#)). The SNRs as an intense source of energetic CREs show a strong magnetic field as previously indicated by [Klein et al. \(1989\)](#). The known SNRs ([Bozzetto et al. 2017](#); [Maggi et al. 2019](#)) are well-matched with the brightest sources of our non-thermal maps.

Table 7 shows the integrated flux densities of the syn-

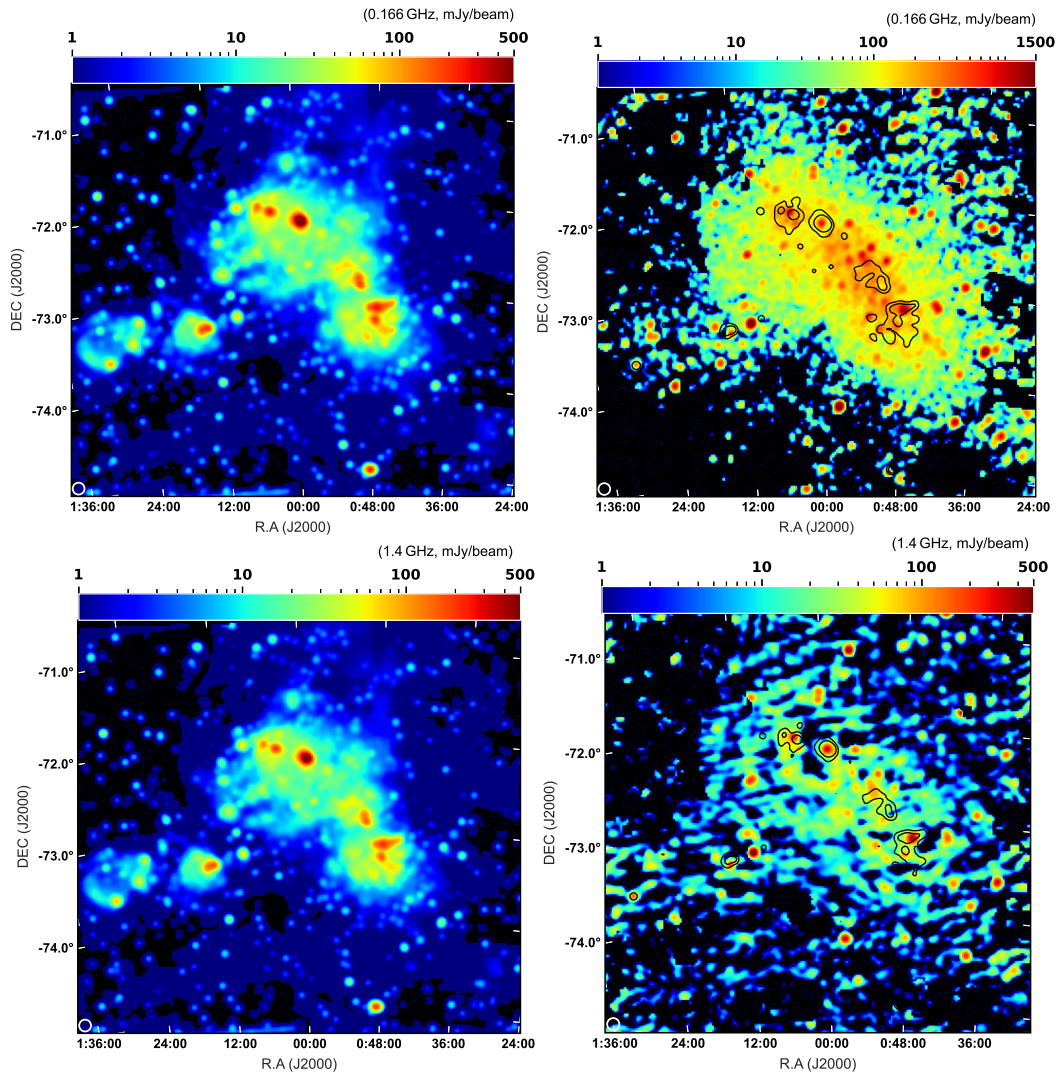


**Figure 6.** The SMC– The thermal free-free (left) and the non-thermal synchrotron (right) emission maps at 0.166 GHz (top) and 1.4 GHz (bottom). Colour bars show the intensities in units of  $\text{mJy beam}^{-1}$  in log scale. The non-thermal maps are overlaid with contours of the thermal emission with levels of 40 and  $100 \text{ mJy beam}^{-1}$ . The beam size of  $235''$  is shown in the lower left corner of the maps.

chrotron and observed RC emission. Integrations were performed from the LMC centre ( $05^{\text{h}} 23^{\text{m}} 34^{\text{s}}, -69^{\circ} 45'22''$ )<sub>J2000</sub> out to the radius of  $R = 5^{\circ}$  and from the SMC centre ( $00^{\text{h}} 52^{\text{m}} 44^{\text{s}}, -72^{\circ} 49'42''$ )<sub>J2000</sub> out to  $R = 3^{\circ}$ . We note that negative map pixels are neglected in these calculations. Otherwise, these pixels reduce the integrated flux density of the observed radio continuum emission by at most 30–35 per cent at 0.166 GHz in both the LMC and the SMC and at 1.4 GHz in the SMC, resulting in an artificial increase in the thermal fraction by about 15 per cent (see Section 4.3). For comparison, the integrated flux densities are reported before and after subtracting background radio sources presented by Filipović et al. (2021) and Payne et al. (2004). These sources account for 53 per cent, 14 per cent, and 4 per cent of the total RC flux at 0.166, 1.4, and 4.8 GHz, respectively in the LMC, indicating that they are mostly steep radio sources ( $\alpha < -1.1$ ). However, we note that as most of these sources are behind the face of the LMC, and hence mixed with the galaxies' extended emission, the resolution at which this subtraction is performed becomes important.

Table 7 shows that the source subtraction from the 1.4 and 4.8 GHz maps results in lower galaxies' integrated fluxes (or higher fluxes of background sources at this frequency leading to their flatter spectra) at the GLEAM resolutions ( $221''$  and  $235''$ ) than at their own native resolutions ( $\leq 40''$  for the LMC and  $98''$  for the SMC, see Table 2). This indicates that subtracting the sources from the GLEAM maps at 0.166 GHz also removes a portion of the extended emission of the galaxies. Hence, studies of the spectral index at which the source subtracted maps/fluxes at different frequencies are used is actually sensitive to the resolution at which the subtraction is performed (see Section 5).

### 4.3 Thermal fraction

The thermal fraction  $f_{\text{th}}$  maps are obtained by dividing the thermal emission by the observed RC at each frequency (Fig. 7). The prominent regions emitting strong free-free emission are H II regions with a median thermal fraction of  $f_{\text{th}}^{0.166 \text{ GHz}} = (49 \pm 9)$  for the LMC and  $f_{\text{th}}^{0.166 \text{ GHz}} = (32 \pm 5)$  per cent for the

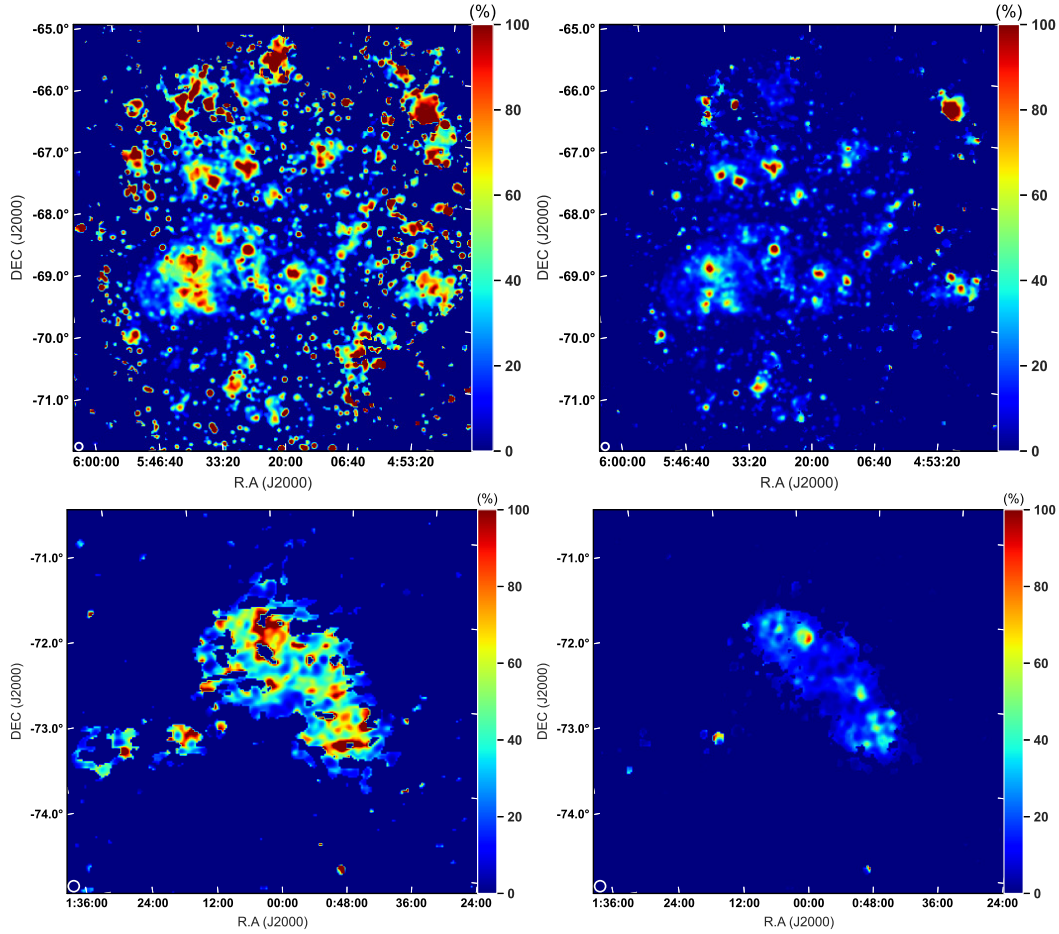


**Figure 7.** Maps of the thermal fraction for the LMC (top) and the SMC (bottom) at 0.166 GHz (left) and 1.4 GHz (right). Colour bars show the fractions in percentage. The beam sizes of  $221''$  (for the LMC) and  $235''$  (for the SMC) are shown in the lower left corner of the maps.

SMC at 0.166 GHz. The H II regions have a higher thermal fraction at 1.4 GHz with a median  $f_{\text{th}}^{1.4\text{ GHz}} = (75 \pm 9)$  per cent for the LMC and  $f_{\text{th}}^{1.4\text{ GHz}} = (79 \pm 10)$  per cent for the SMC. Tables 4 and 5 list  $f_{\text{th}}^{0.166\text{ GHz}}$  and  $f_{\text{th}}^{1.4\text{ GHz}}$  for the individual H II regions.

The global thermal fraction obtained above  $5\sigma$  RMS level of the thermal emission is  $f_{\text{th}}^{1.4\text{ GHz}} = (30 \pm 4)$  per cent in the LMC and slightly higher ( $35 \pm 7$ ) per cent in the SMC at 1.4 GHz. In both galaxies, the thermal fraction at 0.166 GHz is less than 15 per cent. The lower thermal fraction at lower frequencies is expected due to a faster increase of the synchrotron emission than the thermal emission. The MCs' global thermal fractions are higher compared with those of spiral galaxies such as M 33, ( $f_{\text{th}} \sim 18$  per cent) and NGC 6946 ( $f_{\text{th}} \sim 7$  per cent) at 1.4 GHz (Tabatabaei et al. 2008; Tabatabaei et al. 2013a). However, they are lower than those estimated using the classical separation method, i.e., using a fixed spectral index, in the same galaxies (e.g.,  $f_{\text{th}}^{1.4\text{ GHz}} \simeq 55$  per cent in the LMC assuming  $\alpha_n = -0.84$ , Klein et al. 1989). This assumption particularly leads to an excess thermal emission in H II regions. Previously, Klein et al. (1989) indicated that 30 Dor complex is mostly thermal (or at least at 1.4 GHz), however, we find strong non-thermal emission as well.

## 5 Non-thermal Spectral Index

The TRT separation technique used is independent of the synchrotron spectrum and free from any related assumption. Its products at several frequencies can be used to investigate variations in the non-thermal radio spectral index. The synchrotron emission is characterized by a power-law spectrum with an index  $\alpha_n$ ,  $S_n \simeq \nu^{\alpha_n}$ . We map  $\alpha_n$  of the MCs between 0.166 GHz and 1.4 GHz using the non-thermal maps at the corresponding frequencies. This map as well as that of the observed spectral index  $\alpha$ ,  $S \simeq \nu^\alpha$  are derived only for pixels with intensities higher than  $5\sigma$  RMS noise in the MCs. Both the LMC and the SMC show regions of steep spectrum ( $\alpha < -0.8$ , dark blue regions in Figs. 9 and 10), which mostly belong to diffuse parts of the ISM. In massive star-forming regions, the spectrum, even that of the pure synchrotron emission, is relatively flat ( $-0.7 \lesssim \alpha_n \lesssim -0.4$ ), indicating the presence of high energy CREs in these regions. The flattest spectrum is found in the giant H II complex 30 Dor in the LMC.

To obtain an average value of the spectral index, it is essential first to subtract the background radio sources at different frequencies. As discussed in Section 4.2, the final result can change depending on the resolution that subtraction

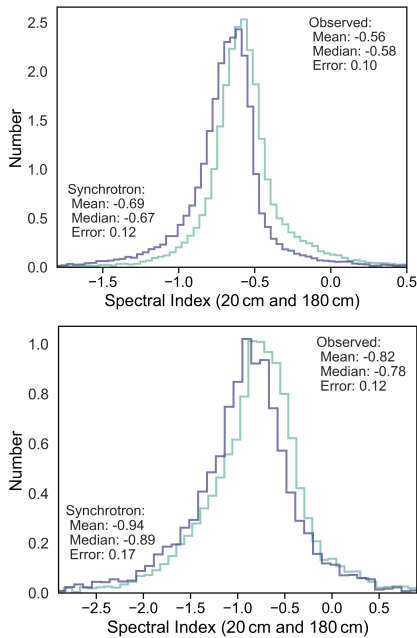


**Figure 8.** Histograms of the spectral index of the observed RC emission  $\alpha$  (green) and its synchrotron component  $\alpha_n$  (purple) measured between 0.166 GHz and 1.4 GHz in the LMC (top) and the SMC (bottom). Vertical axes show the number of pixels in the spectral index maps corresponding to bins of equal width of  $\alpha$  or  $\alpha_n$  values. The intensity maps were subtracted for background radio sources before deriving the  $\alpha$  and  $\alpha_n$  maps.

**Table 7.** The effect of background source subtraction on the integrated flux densities of the observed RC ( $S$ ) and the non-thermal ( $S_{nt}$ ) emission for the LMC ( $R \leq 5^\circ$ ) and the SMC ( $R \leq 3^\circ$ ).

$\nu$ (GHz)	$S$ (Jy)	$S_{nt}$ (Jy)
LMC		
0.166 <sup>a</sup>	1353 ± 138	1179 ± 130
0.166 <sup>b</sup>	641 ± 70	467 ± 51
1.4 <sup>a</sup>	449 ± 30	304 ± 22
1.4 <sup>b</sup>	385 ± 26	240 ± 18
1.4 <sup>c</sup>	242 ± 16	97 ± 7
4.8 <sup>a</sup>	361 ± 31	232 ± 21
4.8 <sup>b</sup>	347 ± 29	218 ± 22
4.8 <sup>c</sup>	231 ± 20	102 ± 9
SMC		
0.166 <sup>a</sup>	260 ± 35	238 ± 33
0.166 <sup>b</sup>	126 ± 17	104 ± 14
1.4 <sup>a</sup>	49.7 ± 6.3	32 ± 4
1.4 <sup>b</sup>	30.2 ± 3.9	12.5 ± 1.7
1.4 <sup>c</sup>	18.9 ± 2.5	1.2 ± 0.2

*a*– Background sources not subtracted. *b*– Background sources subtracted at native resolutions (see Table 2). *c*– Background sources subtracted after convolution to the GLEAM resolutions.

performed. Hence, to keep the residual structures consistent at different frequencies, we have to subtract the sources at the same resolution as of the GLEAM data at 0.166 GHz. In other words, at 1.4 GHz, the maps are first convolved to the GLEAM resolution then subtracted for the sources. We note that this way, the spectral index measurement is accurate, but the ISM regions with a background source behind

**Table 8.** Mean physical properties of the magneto-ionic plasma in the MCs.

Object	$B_{tot}$ ( $\mu\text{G}$ )	$\langle n_e \rangle$ ( $\text{cm}^{-3}$ )	$\beta$
LMC	$10.1 \pm 1.7$	$0.06 \pm 0.01$	$0.06 \pm 0.01$
SMC	$5.5 \pm 1.3$	$0.020 \pm 0.019$	$0.06 \pm 0.06$

are excluded which is unavoidable due to the large beam of the GLEAM data. Fig. 8 shows a histogram of  $\alpha$  and  $\alpha_n$  obtained using the background radio source subtracted intensity maps at 0.166 GHz and 1.4 GHz. We found that both  $\alpha$  and  $\alpha_n$  are flatter in the LMC ( $\alpha = -0.58 \pm 0.10$  and  $\alpha_n = -0.67 \pm 0.12$ ) than in the SMC ( $\alpha = -0.78 \pm 0.12$  and  $\alpha_n = -0.89 \pm 0.17$ ) that is mainly due to the presence of 30 Dor and the fact that the LMC hosts more giant H II regions with flat spectrum than the SMC.

Using all multi-frequency RC maps and archival data available, we further obtain  $\alpha_n$  globally over a wider range of frequencies by modeling the integrated RC spectrum from 0.02 GHz to 8.5 GHz in the LMC and 0.08 GHz to 8.5 GHz in the SMC. All maps are integrated out to the radius of  $5^\circ$  for the LMC and  $3^\circ$  for the SMC from their centres (see Table 1). Tables 9 and 10 summarize our integrated flux measurements ‡ as well as measurements from the literature.

Assuming that the thermal emission is optically thin, the RC spectrum can be expressed as:

$$S_\nu = S_\nu^{\text{th}} + S_\nu^{\text{nt}} = A_1 \nu^{-0.1} + A_2 \nu^{\alpha_n}, \quad (9)$$

where  $A_1$  and  $A_2$  are constant scaling factors. To avoid dependencies on the units of the frequency space, this equation can be written as:

$$S_\nu = A'_1 \left(\frac{\nu}{\nu_0}\right)^{-0.1} + A_2 \nu_0^{\alpha_n} \left(\frac{\nu}{\nu_0}\right)^{\alpha_n}, \quad (10)$$

with  $A'_1 = \nu_0^{-0.1} A_1$  and  $\nu_0$  a reference frequency. Following Tabatabaei et al. (2017), we fit this model to the observed data using the Markov chain Monte Carlo (MCMC) Bayesian method as it provides robust statistical constraints on the fit parameters  $\alpha_n$ ,  $A'_1$  and  $A_2$ . The priors and related model library are set by generating random combinations of the parameters sampled uniformly in wide ranges of parameter space ( $-1 < A'_1, A_2 < 2000$  for the LMC and  $-1 < A'_1, A_2 < 400$  for the SMC§ and  $0 < \alpha_n < 2.2$  Tabatabaei et al. 2017). The parameters  $A'_1$  and  $A_2$  are set to fit the integrated flux densities in unites of Jy.

Figs. 11 and 12 show the resulting fit to the integrated flux densities and the posterior probability distribution function (PDF) of the parameters, respectively.

We obtain a global non-thermal spectral index  $\alpha_n = -0.65 \pm 0.04$  in the LMC and  $-0.74 \pm 0.04$  in the SMC using a reference frequency of  $\nu_0 = 0.166$  GHz. These results agree with the median of the  $\alpha_n$  distribution in the maps presented above. Moreover, we find a good match with the results of

‡ In Tables 9 and 10, the integrations refer to  $> 3\sigma$  level of the RC maps leading to slightly lower values than those listed in Table 7. § We note that negative values of flux density are not physically motivated but are included to assess the robustness of the final results.

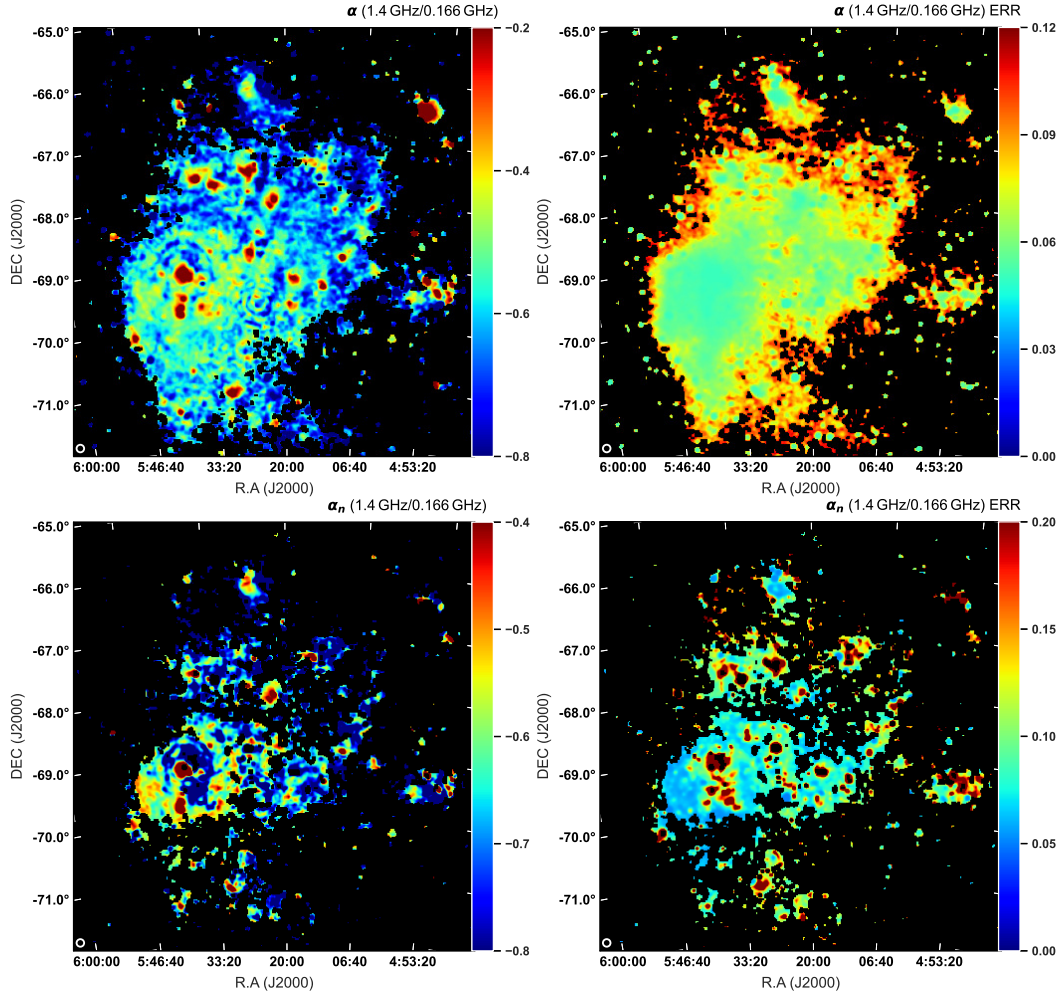


**Figure 9.** Maps of the spectral index (left) and its uncertainty (right) of the observed RC ( $\alpha$ , top) and synchrotron emission ( $\alpha_n$ , bottom) measured between 0.166 GHz and 1.4 GHz for the LMC. The beam size of  $221''$  is shown in the lower left corners.

For et al. (2018) studying the integrated RC SEDs. Our fitting process suggests a curve line for the LMC, which agrees with the best-fit model suggested by For et al. (2018). The curvature shows that both the thermal and non-thermal components are indeed necessary to explain the RC spectrum in the LMC. The non-thermal emission is dominated at lower frequencies and the thermal emission at higher frequencies. In the SMC, however, the non-thermal emission dominates the RC spectrum at the selected frequency range that also agrees with For et al. (2018).

## 6 Discussion

After mapping the extinction and de-reddening the  $H\alpha$  emission, we presented the distribution of the thermal and non-thermal components of the radio continuum emission across the MCs. In this section, we first derive total magnetic field strength, compare the thermal and magnetic energy densities, and investigate a possible correlation between the magnetic field and massive star formation. Moreover, we compare different cooling mechanisms of the CREs in the MCs.

### 6.1 Magnetic field strength

Assuming equipartition between the energy densities of the magnetic field and cosmic-rays (CRs) and using synchrotron intensity ( $I_n$ ), the total magnetic field strength can be derived (e.g., Tabatabaei et al. 2008; Beck & Krause 2005):

$$B_{\text{tot}} = C(\alpha_n, K, L) I_n^{\frac{1}{\alpha_n+3}} \quad (11)$$

Where  $C$  is the function of the non-thermal spectral index,  $K$  the ratio between the number densities of cosmic-ray protons and electrons, and  $L$  is the synchrotron emitting medium's pathlength. Assuming a fixed  $K = 100$  (Beck & Krause 2005), yields maps of the total magnetic field strength (Fig. 13).

Using our non-thermal maps, the mean non-thermal spectral index  $\alpha_n = -0.67$ , and a synchrotron pathlength of  $L = 530 \text{ pc}$  (Gaensler et al. 2005) in the LMC, we derive a mean total magnetic field  $B_{\text{tot}} = 10.1 \pm 1.7 \mu\text{G}$  with errors the uncertainties in the non-thermal intensity and  $\alpha_n$  propagated. This is higher than the previous equipartition estimate given by Klein et al. (1989). The magnetic field is maximum in 30 Dor,  $B_{\text{tot}} = 45 \pm 7 \mu\text{G}$ , but few other H II regions such as N48B and N63A also show the presence of strong magnetic fields. We note that the synchrotron intensity measures

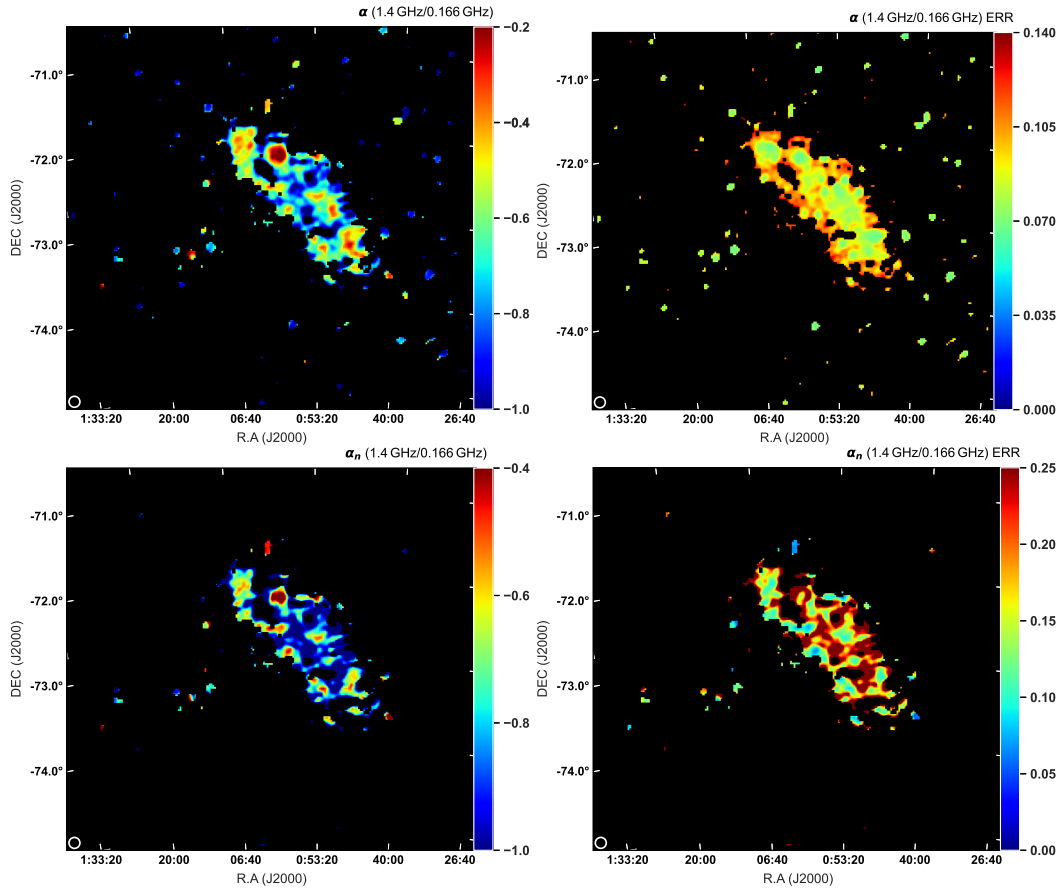


**Figure 10.** Maps of the spectral index (left) and its uncertainty (right) of the observed RC ( $\alpha$ , top) and synchrotron emission ( $\alpha_n$ , bottom) measured between 0.166 GHz and 1.4 GHz for the SMC. The beam size of  $235''$  is shown in the lower left corners.

the total magnetic field perpendicular to the line of sight. The magnetic field along the line of sight is about  $4.3 \mu\text{G}$  as estimated by Gaensler et al. (2005) using the Faraday rotation measures. Our equipartition assumption agrees with Mao et al. (2012) who showed that this condition holds in the LMC using energy density of cosmic-ray with an ordinary cosmic-ray proton to electron ratio  $K = 100$  and an upper limit of  $B_{\text{tot}} = 7 \mu\text{G}$ .

For the SMC, large uncertainties are found with measurements of  $L$  in literature. Assuming a 1 kpc thick-disk for this galaxy,  $L = 1 \text{ kpc} \times \cos(i)^{-1} = 2 \text{ kpc}$ , we obtain total magnetic field strength  $B_{\text{tot}} = 5.5 \pm 1.3 \mu\text{G}$  using  $\alpha_n = -0.89$  that agrees with Loiseau et al. (1987). However, adoption of a lower inclination  $i = 40^\circ$  from Stanimirović et al. (2004), decreases the magnetic field strength by 10 per cent in the SMC. The total magnetic field strength is higher than that Mao et al. (2008) presented. It also appears that the magnetic field of the SMC is much more dominated by diffuse synchrotron emission more than the LMC. Previous studies also show (total) magnetic field strength in dwarf galaxies is about three times weaker than in spiral galaxies (Chyży et al. 2011).

We note that assuming revised minimum energy formula following Beck & Krause (2005), does not change total magnetic field strength significantly (less than 5 per cent). The total magnetic field strength obtained from TRT’s non-thermal emission is higher than using “classical” non-thermal maps.

Using a fixed radio spectral index for separation in all regions (including H II regions) causes lower non-thermal emission and hence underestimates magnetic field strength.

## 6.2 Thermal vs magnetic energy density

The corrected H $\alpha$  emission or the thermal free-free emission is an ideal tracer of the density of thermal electrons  $n_e$  (Condon 1992). The emission measure  $EM$  of the thermal emission is related to  $n_e$  as  $EM = \int n_e^2 dl = \langle n_e^2 \rangle L$ , with  $L$  the line-of-sight pathlength of the ionized medium<sup>¶</sup>. The volume-averaged electron density along the line of sight is given by  $\langle n_e \rangle = \sqrt{f \langle n_e^2 \rangle}$ , with  $f$  the volume filling factor describing the fluctuations in  $n_e$  ( $f \simeq 5$  per cent following Gaensler et al. 2008; Ehle & Beck 1993).

A large variation in  $\langle n_e \rangle$  is obtained in the LMC ranging from  $0.01 \text{ cm}^{-3}$  in weak diffuse regions to higher than  $1 \text{ cm}^{-3}$  in dense areas of 30 Dor with a mean of  $0.045 \text{ cm}^{-3}$  (median  $0.033 \text{ cm}^{-3}$ ). Considering only 30 Dor, we obtain  $\langle n_e \rangle = 0.30 \pm 0.01$  on average. Assuming  $L = 530 \text{ pc}$ , the mean volume-averaged electron density density increases to  $0.062 \text{ cm}^{-3}$  that agrees with the distribution modeling of Yao et al. (2017).

For the SMC, we obtain  $\langle n_e \rangle = 0.020 \pm 0.019 \text{ cm}^{-3}$  with

<sup>¶</sup> It is assumed to be the same as of the magneto-ionic medium (Section 6.1).

**Table 9.** Integrated flux density ( $S_\nu$ ) and uncertainty in flux density ( $\sigma$ ) of the LMC.

$\nu$ (MHz)	$S_\nu$ (Jy)	$\sigma$ (Jy)	Reference
20	5270	1054	Shain (1959) <sup>1</sup>
45	2997	450	Alvarez et al. (1987)
76	1857	315.7	For et al. (2018) <sup>1</sup>
84	1743.3	296.4	For et al. (2018) <sup>1</sup>
85	3689	400	Mills (1959) <sup>2</sup>
92	1619.7	275.3	For et al. (2018) <sup>1</sup>
97	2839	600	Mills (1959) <sup>2</sup>
99	1511.3	256.9	For et al. (2018) <sup>1</sup>
107	1853.7	315.1	For et al. (2018) <sup>1</sup>
115	1646.4	279.9	For et al. (2018) <sup>1</sup>
123	1614.1	274.4	For et al. (2018) <sup>1</sup>
130	1580.3	268.6	For et al. (2018) <sup>1</sup>
143	1670.3	284	For et al. (2018) <sup>1</sup>
150	1406	239	For et al. (2018) <sup>1</sup>
158	1267	215.4	For et al. (2018) <sup>1</sup>
158	1736	490	Mills (1959) <sup>2</sup>
166	1125.7	191.4	For et al. (2018) <sup>1</sup>
174	1334.2	226.8	For et al. (2018) <sup>1</sup>
181	1235.4	210	For et al. (2018) <sup>1</sup>
189	1245.9	211.8	For et al. (2018) <sup>1</sup>
197	1070.2	181.9	For et al. (2018) <sup>1</sup>
204	1247.8	212.1	For et al. (2018) <sup>1</sup>
212	1086	184.6	For et al. (2018) <sup>1</sup>
219	1033.6	175.7	For et al. (2018) <sup>1</sup>
227	997	169.5	For et al. (2018) <sup>1</sup>
408	925	30	Klein et al. (1989)
1400	478.9	30	Klein et al. (1989) <sup>1</sup>
1400	426.1	30	Hughes et al. (2007) <sup>1</sup>
2400	331	50	Filipovic et al. (1996b) <sup>1</sup>
4750	351.5	40	Haynes et al. (1991) <sup>1</sup>
4750	343.5	40	Dickel et al. (2005) <sup>1</sup>
8550	268.3	40	Haynes et al. (1991) <sup>1</sup>
8550	263	40	Dickel et al. (2005) <sup>1</sup>

Notes.

<sup>1</sup>Re-integrated for  $R \leq 5^\circ$ .<sup>2</sup>Revised by Klein et al. (1989).

error the standard deviation. This agrees with Mao et al. (2008) deriving a mean electron density of  $0.039 \text{ cm}^{-3}$  using the pulsar dispersion measure technique.

To address the energy balance in the magneto-ionic ISM of the MCs, the thermal energy density ( $E_{th} = \frac{3}{2}(n_e)kT_e$ ) is compared with the magnetic energy density ( $E_B = B^2/8\pi$ ) for the warm ionized gas  $T_e \simeq 10^4 \text{ K}$ . The energy density of the hot ionized gas with  $T_e \simeq 10^6 \text{ K}$  and an electron density of  $\simeq 0.01(n_e)$  is about the same order of magnitude as the warm ionized gas energy density assuming the pressure equilibrium between the warm and hot ionized gas (e.g., Ferrari 1998). On average, the resulting magnetic energy density is larger than the thermal energy density by about one order of magnitude in both the LMC and the SMC. This means that the ionized ISM is a low-beta plasma ( $\beta \equiv E_{th}/E_B < 1$ ) in these galaxies. In other words, the ionized ISM is magnetically confined to electron densities of  $\langle n_e \rangle = 0.06 \pm 0.01$  in the LMC and  $\langle n_e \rangle = 0.020 \pm 0.019$  in the SMC. Moreover, the total non-thermal pressure inserted from both CREs and magnetic fields (it is twice the magnetic pressure in case of equipartition) dominates the thermal pressure in the ionized phase of the ISM. We summarize magneto-ionic plasma physical properties of the MCs in Table 8.

**Table 10.** Integrated flux density ( $S_\nu$ ) and uncertainty in flux density ( $\sigma$ ) of the SMC.

$\nu$ (MHz)	$S_\nu$ (Jy)	$\sigma$ (Jy)	Reference
76	356.2	96.2	For et al. (2018) <sup>1</sup>
84	272.5	73.6	For et al. (2018) <sup>1</sup>
85.5	460	200	Mills (1959) <sup>2</sup>
92	233	62.9	For et al. (2018) <sup>1</sup>
99	239.6	64.7	For et al. (2018) <sup>1</sup>
107	330.2	89.1	For et al. (2018) <sup>1</sup>
115	246.5	66.5	For et al. (2018) <sup>1</sup>
123	240.4	64.9	For et al. (2018) <sup>1</sup>
130	228.4	61.7	For et al. (2018) <sup>1</sup>
143	304.7	82.3	For et al. (2018) <sup>1</sup>
150	250.3	67.6	For et al. (2018) <sup>1</sup>
158	245	66.2	For et al. (2018) <sup>1</sup>
166	198.8	53.7	For et al. (2018) <sup>1</sup>
174	352.1	95.1	For et al. (2018) <sup>1</sup>
181	275.8	74.5	For et al. (2018) <sup>1</sup>
189	249.6	67.4	For et al. (2018) <sup>1</sup>
197	240	64.8	For et al. (2018) <sup>1</sup>
204	283.6	76.6	For et al. (2018) <sup>1</sup>
212	223.4	60.3	For et al. (2018) <sup>1</sup>
219	216.7	58.5	For et al. (2018) <sup>1</sup>
227	208.1	56.2	For et al. (2018) <sup>1</sup>
408	133	10	Loiseau et al. (1987)
1400	35	6	Wong et al. (2011a) <sup>1</sup>
1400	41.2	6	Haynes et al. (1991) <sup>1</sup>
2450	25.6	7	Haynes et al. (1991) <sup>1</sup>
4750	18.1	5	Haynes et al. (1991) <sup>1</sup>
8550	12.4	5	Haynes et al. (1991) <sup>1</sup>

Notes.

<sup>1</sup>Re-integrated for  $R \leq 3^\circ$ .<sup>2</sup>Revised by Loiseau et al. (1987).

### 6.3 Magnetic field–star formation rate correlation

Studies show that the magnetic field scales with recent SFR globally in galaxies following a power-law index of about  $\gamma = 0.3$  (e.g., Heesen et al. 2014; Chyży et al. 2011; Tabatabaei et al. 2017). That is linked to the amplification of the magnetic field in star-forming regions (Siejkowski et al. 2018; Gressel et al. 2008). However, deviations are found on local scales (e.g., Chyży 2008; Tabatabaei et al. 2013a). It is hence important to dissect the role of the diffuse ISM and spatial resolution in these studies. Thanks to their proximity, the MCs are ideal for testing this correlation at different resolutions down to  $\sim 50 \text{ pc}$ . It is shown that the  $70 \mu\text{m}$  infrared emission can well trace the recent star formation (over the last 100 Myr) in the MCs via the following relation Lawton et al. (2010) that is calibrated for the H II regions in the MC:

$$\left(\frac{\text{SFR}_{70 \mu\text{m}}}{\text{M}_\odot \text{ yr}^{-1}}\right) = 9.7 \times 10^{-44} \left(\frac{L_{70 \mu\text{m}}}{\text{erg s}^{-1}}\right) \quad (12)$$

We investigate the B–SFR correlation by separating the diffuse ISM from star-forming regions at different resolutions. Using  $U_{\text{min}}$  maps from Chastenot et al. (2019), we consider star-forming regions in the LMC ( $U_{\text{min}} > 0.4$ ) and the SMC

( $U_{\min} > 0.5$ ). The correlation between magnetic field strength and  $70\ \mu\text{m}$  SFR is obtained through a beam independent spacing, yielding Pearson correlation coefficient  $r \sim 0.6$  in the LMC and the SMC. The B vs SFR can best be explained by a power-law relation with an index  $\gamma$  fitted using the bisector OLS [Isobe et al. \(1990\)](#) regression (Table 11). Fig. 14 present the correlation of B with SFR in spatial resolution of 53 pc for the LMC and 71 pc for the SMC.

We find that B and SFR traced by the  $70\ \mu\text{m}$  are correlated in the SF regions at all selected resolutions. In the LMC, the power-law exponent agrees with the theoretical turbulent amplification value ([Schleicher & Beck 2013](#)). However, in the SMC, it is slightly lower at the original resolution. As expected, no correlation holds in the diffuse ISM at the native resolution. However, it is interesting to note that this correlation is increased at lower resolutions due to mixing with the SF regions. The exponent of  $\gamma_{\text{LMC}} = 0.24 \pm 0.01$  and  $\gamma_{\text{SMC}} = 0.20 \pm 0.01$  obtained is in excellent agreement with global studies of Magellanic-type galaxies with slope  $\gamma = 0.25 \pm 0.02$  given by ([Jurusik et al. 2014](#)). This experiment shows that, in local studies, the power-law exponent can become flatter than the theoretical value because of contamination by the diffuse ISM.

#### 6.4 Cooling of cosmic-ray electrons

The power law energy distribution of CREs  $dN/dE \propto E^{-\beta}$  where  $\beta$  is related to the observed spectral index with  $\alpha = -(2\beta - 1)$  could change due to various energy loss mechanisms. The non-thermal spectral index becomes steeper due to different energy losses of the CREs' diffusion from primary sources (e.g., H II regions). In order to clarify the most effective energy loss mechanism of CREs in H II regions, we study two well-known H II regions in the MCs. We measure the radial profile of the average observed/non-thermal spectral index and thermal fraction centred on ( $05^{\text{h}} 38^{\text{m}} 42^{\text{s}}, -69^{\circ} 06' 03''$ )<sub>J2000</sub> and ( $0^{\text{h}} 59^{\text{m}} 05^{\text{s}}, -72^{\circ} 10' 41''$ )<sub>J2000</sub> in 30 Dor and N66 H II complex respectively using beam independent rings of  $7.2'$  radius in 30 Dor and  $3.91'$  in N66. Fig. 15 shows the radial profile of the spectral index and thermal fraction from the centre of 30 Dor and N66. The spectral index profile of 30 Dor starts with very flat spectrum  $\alpha \sim 0$  in the centre but it drops rapidly moving away from the centre. At a distance of  $R = 0.3\ \text{kpc}$ ,  $\alpha_n$  reaches to a steep value ( $\sim -0.85$ ) and again flattens to about the average galaxy value. The flattening of the synchrotron spectrum around  $R = 0.5\ \text{kpc}$  is most likely due to the ring-like artefact in the observed RC map at 1.4 GHz ([Hughes 2011](#)) which also leads to an artificially higher thermal fraction.

The spectral index of 30 Dor starts to fall off after  $R > 0.5\ \text{kpc}$  due to the diffusion of CREs, but it has again two slight flattening and higher thermal fractions around  $R \sim 1\ \text{kpc}$  and  $R \sim 1.4\ \text{kpc}$ . This can be interpreted as re-acceleration of CREs due to feedback and shock waves from the two nearby H II regions, N144 and N59. Overall, 30 Dor radio spectral index would decrease slightly to the galaxy average value  $\alpha = -0.64$  at the scale of  $R \sim 2\ \text{kpc}$ . Beyond  $R > 2\ \text{kpc}$ , the non-thermal spectral index  $\alpha_n \sim -0.85$ , never attaining to characteristic values of CREs synchrotron losses (i.e.,  $\alpha_n < -1$ , [Biermann & Strom 1993](#)). Similar to 30 Dor, N66 H II complex of the SMC also shows flat val-

ues of  $\alpha = -0.1$  in the core ( $R < 0.1\ \text{kpc}$ ). The non-thermal spectral index  $\alpha_n$  decreases to steeper values of  $\alpha_n < -1$  for  $R < 0.3\ \text{kpc}$  of N66. Such a steep  $\alpha_n$  could be interpreted as CREs energy loss due to synchrotron loss mechanism. However, the measurement suffers from large uncertainties due to the low sensitivity of the radio continuum data at 1.4 GHz. After  $R > 0.3\ \text{kpc}$ , the observed spectral index increases to the mean value of the galaxy, and  $\alpha_n$  does not reach to steeper values than  $< -1$ , indicating that the synchrotron energy loss mechanism is not an efficient cooling mechanism in N66 as well. In order to assess different CREs cooling processes in the core of these H II regions ( $R < 0.2\ \text{kpc}$ ), we estimate their cooling timescale using the equations presented in [Lacki et al. \(2010\)](#):

$$\begin{aligned} \left(\frac{\tau_{\text{syn}}}{\text{yr}}\right) &\approx 4.5 \times 10^7 \left(\frac{B}{10\ \mu\text{G}}\right)^{-3/2} \nu_{\text{GHz}}^{-1/2} \\ \left(\frac{\tau_{\text{ion}}}{\text{yr}}\right) &\approx 2.1 \times 10^8 \left(\frac{B}{10\ \mu\text{G}}\right)^{-1/2} \nu_{\text{GHz}}^{1/2} \left(\frac{n_{\text{eff}}}{\text{cm}^3}\right)^{-1} \\ \left(\frac{\tau_{\text{IC}}}{\text{yr}}\right) &\approx 1.8 \times 10^8 \left(\frac{B}{10\ \mu\text{G}}\right)^{1/2} \nu_{\text{GHz}}^{-1/2} U_{\text{rad},-12}^{-1} \\ \left(\frac{\tau_{\text{brem}}}{\text{yr}}\right) &\approx 3.7 \times 10^7 \left(\frac{n_{\text{eff}}}{\text{cm}^3}\right)^{-1} \\ \left(\frac{\tau_{\text{diff}}}{\text{yr}}\right) &\approx 2.6 \times 10^7 \left(\frac{E}{3\ \text{GeV}}\right)^{-1/2} \end{aligned} \quad (13)$$

Where the effective ISM number density experienced by CRs  $n_{\text{eff}} = f_{\text{ISM}} < n >$  and mean ISM number density within the CREs confinement volume  $< n > = \Sigma_{\text{gas}}/2h$ . We note that CRs traverse in high-density clumpy ISM which is confined by clumps magnetic field experiences a higher  $f_{\text{ISM}} > 1$  in comparison with a low-density diffuse ISM. We assume  $f_{\text{ISM}} = 1$  for the MC.

However, taking higher  $f_{\text{ISM}} > 1$  for the compact H II regions of the MCs, decreases the cooling timescale of bremsstrahlung and ionization losses, making them more effective cooling mechanisms for CR electrons and positrons by propagating away from H II regions. We assume the scale height of CR  $h = 1\ \text{kpc}$ . The radiation energy density  $U_{\text{rad}}$  is obtained from [Draine & Li \(2007\)](#) and corrected for contributions of the cosmic microwave background radiation energy density  $U_{\text{CMB}} = 4.17 \times 10^{-13}\ \text{erg cm}^{-3}$  and dust emission energy density  $U_{\text{FIR}} = 5 \times 10^{-13}\ \text{erg cm}^{-3}$  ([Tabatabaei et al. 2013a](#); [Draine 2011](#)). In order to determine the diffusion timescale, the most energetic CR electrons emit at a critical frequency  $\nu_c$  obtained from [Murphy et al. \(2012\)](#):

$$\left(\frac{E}{\text{GeV}}\right) = 8.8 \left(\frac{\nu_c}{\text{GHz}}\right)^{1/2} \left(\frac{B}{\mu\text{G}}\right)^{-1/2} \quad (14)$$

Out to the radius of 200 pc from 30 Dor central point, total magnetic field strength map yields an average  $B_{\text{tot}} = 26.43\ \mu\text{G}$  and corresponding CR electron energy  $\sim 3.8\ \text{GeV}$  at 4.8 GHz. We found the average number density of the ISM experienced by the CRs  $n_{\text{eff}} \sim 0.94\ \text{cm}^{-3}$  and average total radiation energy density  $U_{\text{rad}} = 5.06 U_{\odot}$  in 30 Dor. These estimation suggests that synchrotron escape is the dominant cosmic-ray loss mechanism in 30 Dor core  $\tau_{\text{syn}} \sim 4.7\ \text{Myr}$  and there is a strong competition between Inverse-Compton cooling timescale  $\tau_{\text{IC}} \sim 26.3\ \text{Myr}$  and diffuse cooling  $\tau_{\text{diff}}$

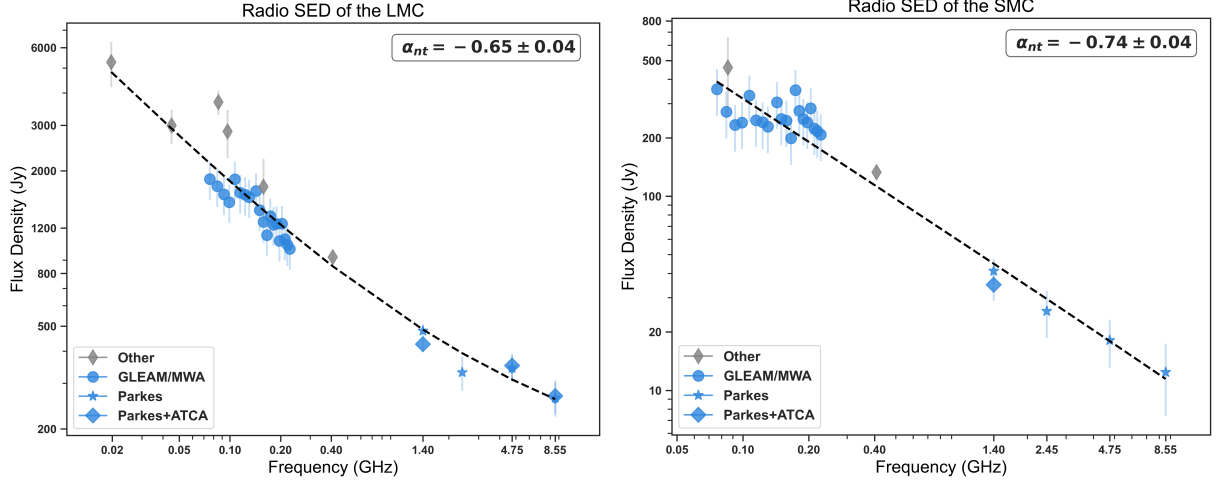


**Figure 11.** The radio continuum spectrum from about 0.02 GHz to 8.5 GHz for the LMC (left) and the SMC (right).

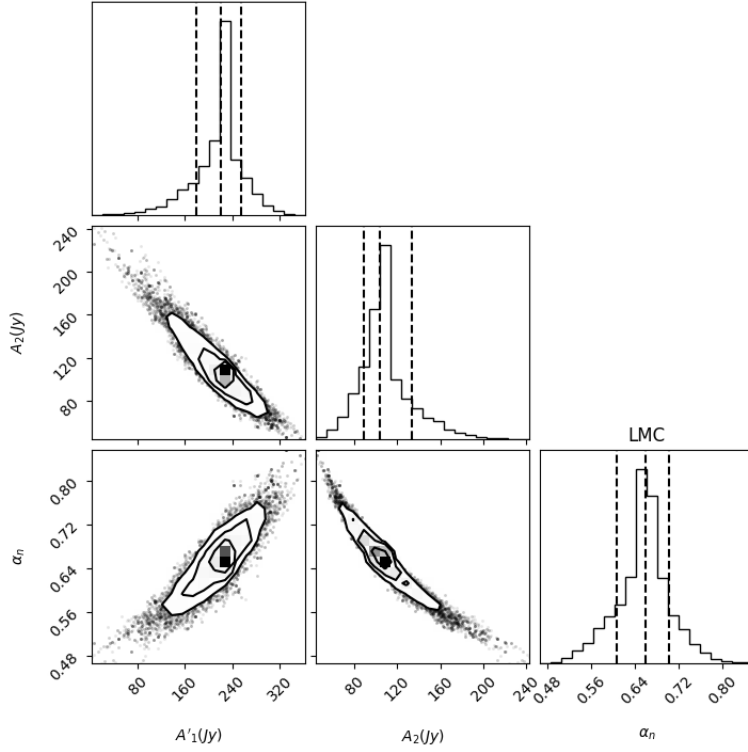


**Figure 12.** Bayesian corner plots for the parameters  $A'_1$  and  $A_2$  in equation (10) showing the posterior PDF and their 0.16, 0.5, and 0.86 percentiles for the LMC. The uncertainty contours show that the posteriors have the highest probability to occur within the confidence intervals indicated.

$\sim 23.2$  Myr for CR, while the ionization cooling has a less cooling effect on CR with a characteristic time scale  $\tau_{\text{ion}} \sim 300.8$  Myr.

Integrating out to the radius of 100 pc from the SMC N66 complex, we found a mean  $B_{\text{tot}} = 8.50 \mu\text{G}$ , CR electron energy  $\sim 3.5$  GeV at 1.4 GHz, and  $n_{\text{eff}} \sim 0.73 \text{ cm}^{-3}$ . The diffuse cooling is the most effective cooling mechanisms with  $\tau_{\text{diff}} \sim 23.8$  Myr for CR in this region. Furthermore, it shows a strong competition between synchrotron escape,  $\tau_{\text{syn}}$

$\sim 48.5$  Myr and Inverse-Compton cooling,  $\tau_{\text{diff}} \sim 45.7$  Myr. Although Ionization loss is the weakest cooling mechanism in the N66, however, taking the contribution of  $H_2$  in the total gas surface density will decrease its cooling time scale.

### 6.5 Recombination scenario

Determining extinction and free-free emission depends on the optical depth of Lyman continuum photons and whether the

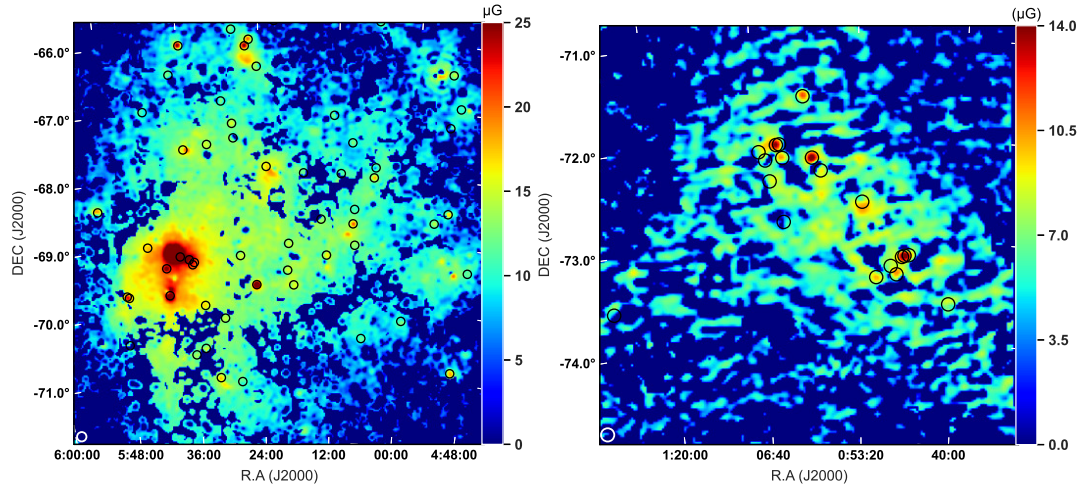


**Figure 13.** Total magnetic field strength of the LMC (left) and the SMC (right) derived using the background source subtracted non-thermal intensity maps at 4.8 GHz in the LMC and at 1.4 GHz in the SMC. Colour bars show the field strength in units of  $\mu\text{G}$ . The beam sizes of  $221''$  (for the LMC) and  $235''$  (for the SMC) are indicated in the lower left corners. Black circles show the position of confirmed SNRs in the LMC and the SMC. (Bozzetto et al. 2017; Maggi et al. 2019).

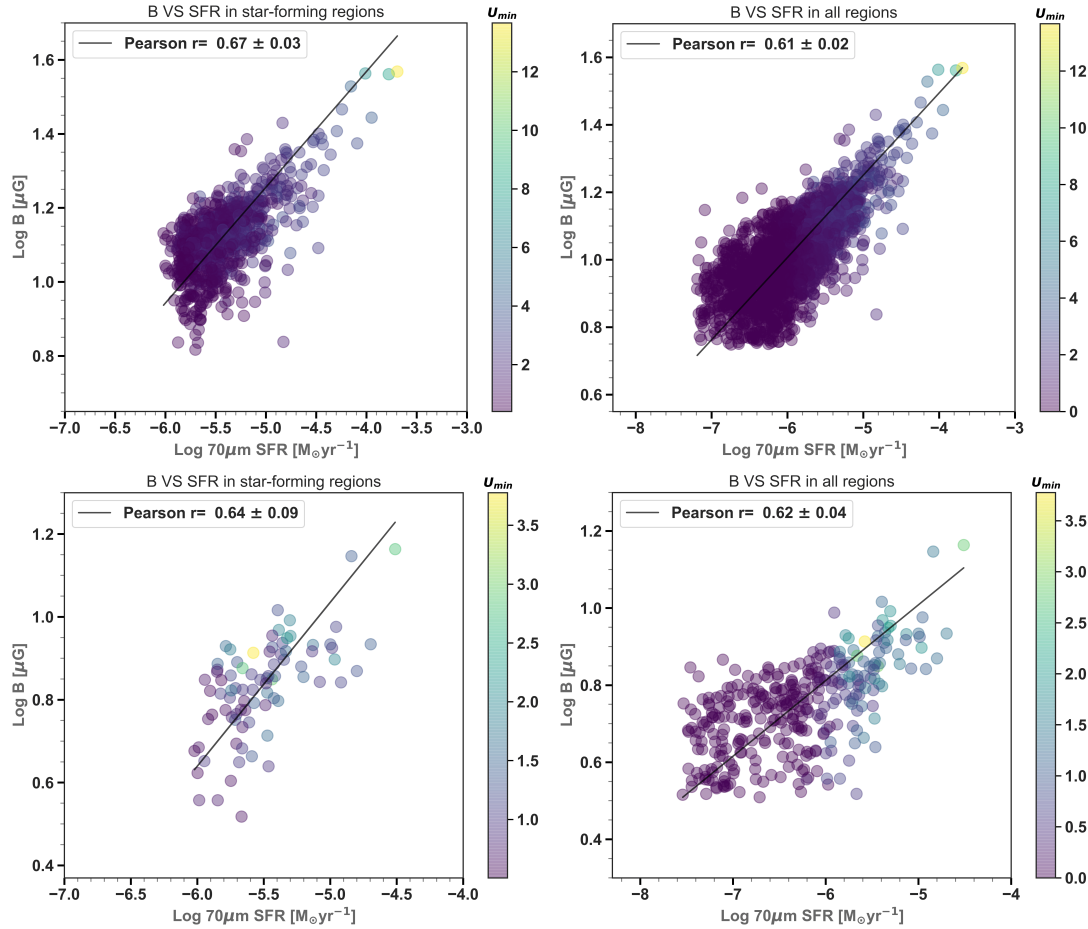


**Figure 14.** Correlation between the total magnetic field strength  $B$  and the  $70\mu\text{m}$  emission as a SFR tracer for the LMC (top) and the SMC (bottom) in star-forming regions (left) as well as all regions above the  $3\sigma$  rms level (right). Solid line shows the bisector fit and the bars indicate  $U_{\text{min}}$  in units of  $U_{\odot}$ .

**Table 11.** Correlation between the magnetic field strength and SFR in different regimes of radiation field (SF, ISRF) at different linear resolutions.

Y	$\gamma^{\text{total}}$	$r_p^{\text{total}}$	$t(n)^{\text{total}}$	$\gamma^{\text{SF}}$	$r_p^{\text{SF}}$	$t(n)^{\text{SF}}$	$\gamma^{\text{ISRF}}$	$r_p^{\text{ISRF}}$	$t(n)^{\text{ISRF}}$
LMC									
B (53 pc)	$0.24 \pm 0.01$	$0.61 \pm 0.02$	159.70(2166)	$0.31 \pm 0.01$	$0.67 \pm 0.03$	116.83(843)	-	$0.39 \pm 0.03$	177.11(1281)
B (150 pc)	$0.28 \pm 0.01$	$0.57 \pm 0.04$	51.95(355)	$0.29 \pm 0.03$	$0.56 \pm 0.08$	42.07(120)	$0.30 \pm 0.02$	$0.49 \pm 0.06$	60.16(235)
B (300 pc)	$0.31 \pm 0.02$	$0.78 \pm 0.08$	22.59(63)	$0.31 \pm 0.04$	$0.70 \pm 0.15$	23.28(26)	$0.30 \pm 0.05$	$0.50 \pm 0.15$	25.36(37)
SMC									
B (71 pc)	$0.20 \pm 0.01$	$0.62 \pm 0.04$	65.18(328)	$0.40 \pm 0.04$	$0.64 \pm 0.09$	32.96(82)	-	$0.38 \pm 0.06$	70.49(246)
B (150 pc)	$0.24 \pm 0.01$	$0.59 \pm 0.07$	38.53(156)	$0.43 \pm 0.11$	$0.53 \pm 0.21$	20.07(19)	$0.28 \pm 0.03$	$0.51 \pm 0.08$	41.46(132)

The linear fit obtained in logarithmic scale ( $\text{Log } Y = \gamma \text{ Log } X$ ) using the bisector least square fit.

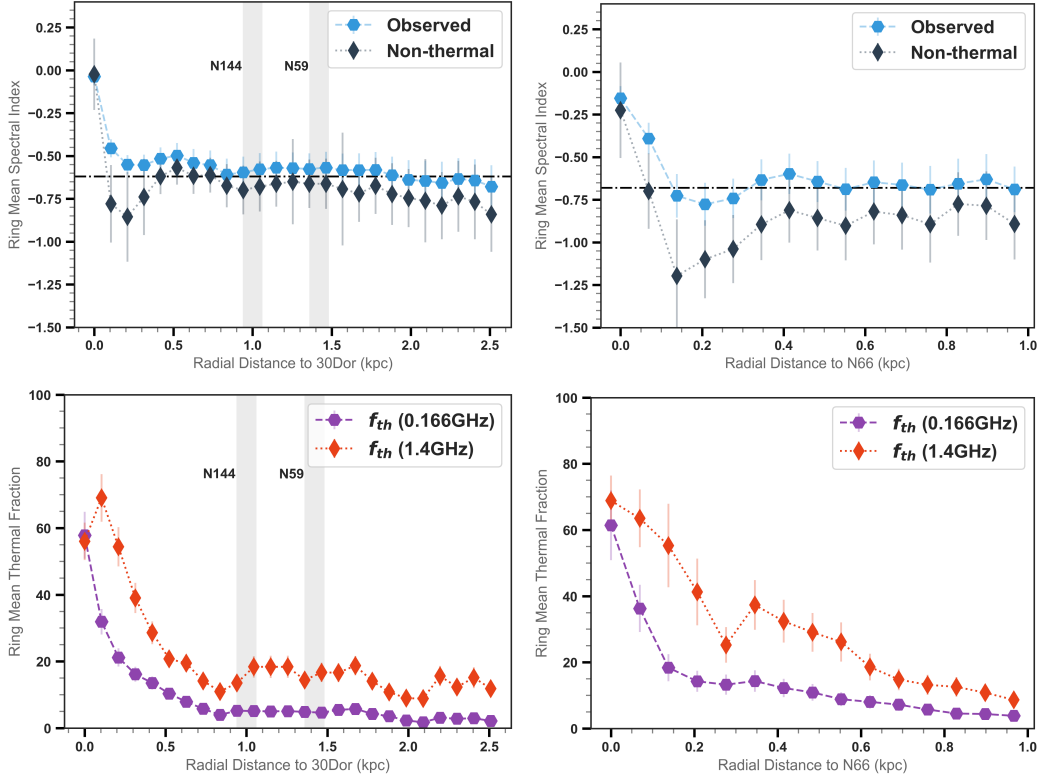


**Figure 15.** Radial profiles of the spectral index (top) and thermal fraction (bottom) in 30 Dor (left) and N66 (right). The dashed horizontal lines in the spectral index profiles indicate the average galaxy values. The vertical grey bands show the position of the 30 Dor’s neighbouring H II regions N144 and N59.

optically thick condition known as Case B recombination or the optically thin scenario known as case A recombination is assumed. Although the theoretical Balmer decrement ratio  $j_{H\alpha}/j_{H\beta} = 2.86$  is almost the same for both scenarios under the assumption of  $T_e = 10,000$  K (Osterbrock 1989), but variation of EM is significant depending on the electron density as well as the optical depth of Lyman continuum photons (Valls-Gabaud 1998). Pellegrini et al. (2012) estimated that the escape fraction of Lyman continuum photons is at least  $f_{\text{esc}} = 0.42$  and  $f_{\text{esc}} = 0.40$  in the H II regions of the LMC and SMC, respectively. Similar results were obtained by Kennicutt et al. (1995), i.e.,  $f_{\text{esc}} = 0.51$ , based on diffuse to total  $H\alpha$  emission flux for the LMC (Oey & Kennicutt 1997). Adopting the case A recombination increases the thermal emission flux by about 49-51 per cent for both the LMC and the SMC

at 0.166 GHz and 1.4 GHz. Consequently, the global magnetic field strength decreases by about 16 per cent.

## 7 Conclusion

Using multi-frequency observations in the radio, FIR, and optical domains, we presented the most precise picture of the distribution of the thermal and non-thermal RC emission in the MCs ever with no use of any assumption about the synchrotron spectral index or extinction. The highly resolved and sensitive Spitzer and Herschel observations have allowed mapping dust mass in galaxies in general. However, using these maps to determine extinction needs a priori assumption about the distribution of ionized gas and dust along the line of sight. Combining the dust mass maps with the data

of the Balmer decrements, we introduced a new method to determine the true fraction of dust that actually attenuates H $\alpha$  emission along the line of sight,  $f_d$ . This fraction is determined for the first time in the MCs in both H II regions and more diffuse regions in the ISM using the MUSE IFU observations. We also presented a calibration relation to map  $f_d$  based on its anti-correlation with the neutral gas surface density. Using the de-reddened H $\alpha$  emission, we derived the free-free emission at 0.166, 1.4, and 4.8 GHz and obtained maps of the non-thermal emission and the pure synchrotron spectral index in the MCs. The latter two maps allowed us to map the strength of the total magnetic field at a spatial resolution of  $\sim 3.7'$  in the LMC and  $\sim 3.9'$  in the SMC. Our results are summarized as follows.

(i) The dust optical depth  $\tau_{\text{dust}}$  is optically thin ( $\tau_{\text{dust}} < 1$ ) to the H $\alpha$  photons in the MCs's diffuse ISM. Whereas total dust mass surface density indicates  $\tau_{\text{dust}}$  ranges between 2–5 in H II regions of the MCs. Only a fraction of this dust mass plays a role in the attenuation of optical waves.

(ii)  $f_d$  is lower in dense star-forming regions ( $\sim 0.1$ ) than in the more diffuse ISM ( $> 0.2$ ). Based on the anti-correlation between  $f_d$  and total gas surface density, we find that the mean  $f_d$  over the entire LMC is about 0.3 that agrees with the Milky Way value.

(iii) The non-thermal fraction is significant at 0.166 GHz with an average value of 80-90 per cent in the diffuse ISM of these galaxies and in massive star-forming regions such as N157. Supernova remnants contribute the most to our 0.166 GHz non-thermal emission map with an average value of non-thermal fraction  $> 85$  per cent. Furthermore, thermal fraction at 1.4 GHz is estimated to be  $f_{\text{th}} = 30$  per cent in the LMC and 35 per cent in the SMC.

(iv) The synchrotron spectrum steepens from massive star-forming regions  $\alpha_n > -0.4$  to the diffuse ISM  $\alpha_n < -0.7$ . This indicates energy loss and cooling of CREs as they propagate away from their birthplaces in SF regions. After injection, CREs can also experience re-acceleration in complexes of SF regions flattening their spectrum as observed in 30 Dor. Comparing different mechanisms, we find that the synchrotron energy loss dominates cooling of CREs in 30 Dor core ( $R < 0.2$  kpc). Using non-thermal maps between 0.166 GHz and 1.4 GHz, we found the median synchrotron spectral index  $\alpha_n = -0.67 \pm 0.12$  and  $\alpha_n = -0.89 \pm 0.17$  in the LMC and the SMC respectively. Using this synchrotron spectral index and equipartition assumption, we found an average total magnetic field strength  $B_{\text{tot}} \simeq 10.1 \mu\text{G}$  in the LMC and  $5.5 \mu\text{G}$  in the SMC.

(v) This study shows that the ISM is dominated by a low-beta plasma given that the thermal energy density is smaller than the non-thermal energy density ( $E_B + E_{\text{CR}}$ ) by more than one order of magnitude.

It is worth mentioning that the present generation of the interferometric radio surveys of the MCs are limited to either low sensitivity caused by instrumental artefacts (particularly at 4.8 GHz and 1.4 GHz) or low resolution (particularly at 0.2 GHz). The limitations in sensitivity can prevent studying the physics of the low-surface brightness ISM which constitutes a major part of low-mass and irregular galaxies such as the MCs. Designing the next generation of the RC surveys, it is important to attain a much larger dynamic range. Technically, limitations in dynamic range can be caused by instrumental artefacts or incomplete calibration of instrumen-

tal response (Braun 2013). As discussed in Section 4.2 and Section 5, the resolution at which background radio sources are subtracted can affect the integrated flux density measurements as well as the spectral index analysis in the MCs. Hence, higher resolution observations are required (particularly at low-frequencies) to disentangle the ISM from the external sources more accurately. The upcoming surveys with the SKA-low can ideally overcome this issue in the MCs. Therefore, following these observational limitations, the main contribution of this paper is in setting a methodology for the unbiased separation of thermal vs non-thermal emission for the upcoming surveys of the MCs and nearby galaxies with the SKA and its pathfinders such as ASKAP and MeerKAT.

### Data availability

The data underlying this article will be shared on reasonable requests.

### Acknowledgements

The authors thank Miroslav D. Filipovic for providing the catalog of the background radio sources in the LMC and also his helpful comments improving the paper. HH thanks the School of Astronomy at the Institute for Research in Fundamental Sciences for its financial support.

### REFERENCES

- Alvarez H., Aparici J., May J., 1987, *A&A*, **176**, 25  
 Bacon R., et al., 2010, The MUSE second-generation VLT instrument. p. 773508, doi:10.1117/12.856027  
 Beck R., Krause M., 2005, *Astronomische Nachrichten*, **326**, 414  
 Biermann P. L., Strom R. G., 1993, *A&A*, **275**, 659  
 Bowman J. D., et al., 2013, *Publications of the Astronomical Society of Australia*, **30**, e031  
 Bozzetto L. M., et al., 2017, *The Astrophysical Journal Supplement Series*, **230**, 2  
 Braun R., 2013, *A&A*, **551**, A91  
 Brocklehurst M., 1971, *MNRAS*, **153**, 471  
 Calzetti D., Armus L., Bohlin R. C., Kinney A. L., Koornneef J., Storchi-Bergmann T., 2000, *ApJ*, **533**, 682  
 Caplan J., Deharveng L., 1985, *A&AS*, **62**, 63  
 Caplan J., Ye T., Deharveng L., Turtle A. J., Kennicutt R. C., 1996, *A&A*, **307**, 403  
 Cardelli J. A., Clayton G. C., Mathis J. S., 1989, *ApJ*, **345**, 245  
 Chasteney J., et al., 2019, *The Astrophysical Journal*, **876**, 62  
 Chyży K. T., 2008, *A&A*, **482**, 755  
 Chyży K. T., Weżgowiec M., Beck R., Bomans D. J., 2011, *A&A*, **529**, A94  
 Condon J. J., 1992, *ARA&A*, **30**, 575  
 Crawford E. J., Filipovic M. D., de Horta A. Y., Wong G. F., Tothill N. F. H., Draskovic D., Collier J. D., Galvin T. J., 2011, *Serbian Astronomical Journal*, **183**, 95  
 Dickel J. R., McIntyre V. J., Gruendl R. A., Milne D. K., 2005, *AJ*, **129**, 790  
 Dickel J. R., Gruendl R. A., McIntyre V. J., Amy S. W., 2010, *The Astronomical Journal*, **140**, 1511  
 Dickinson C., Davies R. D., Davis R. J., 2003, *Monthly Notices of the Royal Astronomical Society*, **341**, 369  
 Draine B. T., 2011, *Physics of the Interstellar and Intergalactic Medium*  
 Draine B. T., Li A., 2007, *ApJ*, **657**, 810

- Dufour R. J., 1975, *ApJ*, **195**, 315
- Dufour R. J., Harlow W. V., 1977, *ApJ*, **216**, 706
- Ehle M., Beck R., 1993, *A&A*, **273**, 45
- Ferrari A., 1998, *Annual Review of Astronomy and Astrophysics*, **36**, 539
- Filipovic M. D., Haynes R. F., White G. L., Jones P. A., Klein U., Wielebinski R., 1995, *A&AS*, **111**, 311
- Filipovic M. D., White G. L., Haynes R. F., Jones P. A., Meinert D., Wielebinski R., Klein U., 1996a, *A&AS*, **120**, 77
- Filipovic M. D., White G. L., Haynes R. F., Jones P. A., Meinert D., Wielebinski R., Klein U., 1996b, *A&AS*, **120**, 77
- Filipovic M. D., Jones P. A., White G. L., Haynes R. F., Klein U., Wielebinski R., 1997, *A&AS*, **121**, 321
- Filipovic M. D., Haynes R. F., White G. L., Jones P. A., 1998, *A&AS*, **130**, 421
- Filipović M. D., et al., 2021, arXiv e-prints, p. [arXiv:2107.10967](https://arxiv.org/abs/2107.10967)
- For B. Q., et al., 2018, *MNRAS*, **480**, 2743
- Gaensler B. M., Haverkorn M., Staveley-Smith L., Dickey J. M., McClure-Griffiths N. M., Dickel J. R., Wolleben M., 2005, *Science*, **307** 5715, 1610
- Gaensler B. M., Madsen G. J., Chatterjee S., Mao S. A., 2008, *Publ. Astron. Soc. Australia*, **25**, 184
- Gordon K. D., Clayton G. C., Misselt K. A., Landolt A. U., Wolff M. J., 2003, *The Astrophysical Journal*, **594**, 279
- Gordon K. D., et al., 2011, *AJ*, **142**, 102
- Graczyk D., et al., 2020, arXiv e-prints, p. [arXiv:2010.08754](https://arxiv.org/abs/2010.08754)
- Gressel O., Elstner D., Ziegler U., Rüdiger G., 2008, *A&A*, **486**, L35
- Haynes R. F., Klein U., Wielebinski R., Murray J. D., 1986, *A&A*, **159**, 22
- Haynes R. F., et al., 1991, *A&A*, **252**, 475
- Heesen V., Brinks E., Leroy A. K., Heald G., Braun R., Bigiel F., Beck R., 2014, *AJ*, **147**, 103
- Helou G., Soifer B. T., Rowan-Robinson M., 1985, *ApJ*, **298**, L7
- Hughes A., 2011, PhD thesis, Swinburne University of Technology
- Hughes A., Wong T., Ekers R., Staveley-Smith L., Filipovic M., Maddison S., Fukui Y., Mizuno N., 2006, *Monthly Notices of the Royal Astronomical Society*, **370**, 363
- Hughes A., Staveley-Smith L., Kim S., Wolleben M., Filipović M., 2007, *Monthly Notices of the Royal Astronomical Society*, **382**, 543
- Hurley-Walker N., et al., 2016, *Monthly Notices of the Royal Astronomical Society*, **464**, 1146
- Isobe T., Feigelson E. D., Akritas M. G., Babu G. J., 1990, *ApJ*, **364**, 104
- Jameson K. E., et al., 2016, *ApJ*, **825**, 12
- Joseph T. D., et al., 2019, *MNRAS*, **490**, 1202
- Jurusik W., Drzazga R. T., Jableka M., Chyży K. T., Beck R., Klein U., Weżgowiec M., 2014, *A&A*, **567**, A134
- Kennicutt Robert C. J., Bresolin F., Bomans D. J., Bothun G. D., Thompson I. B., 1995, *AJ*, **109**, 594
- Kim S., Staveley-Smith L., Dopita M. A., Freeman K. C., Sault R. J., Kesteven M. J., McConnell D., 1998, *The Astrophysical Journal*, **503**, 674
- Kim S., Staveley-Smith L., Dopita M. A., Sault R. J., Freeman K. C., Lee Y., Chu Y.-H., 2003, *ApJS*, **148**, 473
- Klein U., Wielebinski R., Haynes R. F., Malin D. F., 1989, *A&A*, **211**, 280
- Klein U., Haynes R. F., Wielebinski R., Meinert D., 1993, *A&A*, **271**, 402
- Lacki B. C., Thompson T. A., Quataert E., 2010, *ApJ*, **717**, 1
- Lakićević M., et al., 2015, *ApJ*, **799**, 50
- Lawton B., et al., 2010, *ApJ*, **716**, 453
- Leroy A. K., et al., 2011, *ApJ*, **737**, 12
- Loiseau N., Klein U., Greybe A., Wielebinski R., Haynes R. F., 1987, *A&A*, **178**, 62
- Longair M. S., 2011, *High Energy Astrophysics*
- Lonsdale C. J., et al., 2009, *Proceedings of the IEEE*, **97**, 1497
- Maggi P., et al., 2019, *A&A*, **631**, A127
- Mao S. A., Gaensler B. M., Stanimirović S., Haverkorn M., McClure-Griffiths N. M., Staveley-Smith L., Dickey J. M., 2008, *The Astrophysical Journal*, **688**, 1029–1049
- Mao S. A., et al., 2012, *ApJ*, **759**, 25
- McLeod A. F., Dale J. E., Evans C. J., Ginsburg A., Kruijssen J. M. D., Pellegrini E. W., Ramsay S. K., Testi L., 2018, *Monthly Notices of the Royal Astronomical Society*, **486**, 5263–5288
- Meixner M., et al., 2006, *AJ*, **132**, 2268
- Meixner M., et al., 2010, *A&A*, **518**, L71
- Meixner M., et al., 2013, *AJ*, **146**, 62
- Meixner M., et al., 2015, *AJ*, **149**, 88
- Mills B. Y., 1959, *Handbuch der Physik*, **53**, 239
- Murphy E. J., Porter T. A., Moskalenko I. V., Helou G., Strong A. W., 2012, *ApJ*, **750**, 126
- Oey M. S., Kennicutt R. C. J., 1997, *MNRAS*, **291**, 827
- Oster L., 1961, *Rev. Mod. Phys.*, **33**, 525
- Osterbrock D. E., 1989, *Astrophysics of gaseous nebulae and active galactic nuclei*
- Paredes L., Points S. D., Smith R. C., Rest A., Damke G., Zenteno A., MCELS Team 2015, in Points S., Kunder A., eds, *Astronomical Society of the Pacific Conference Series Vol. 491, Fifty Years of Wide Field Studies in the Southern Hemisphere: Resolved Stellar Populations of the Galactic Bulge and Magellanic Clouds*. pp 366–369
- Payne J. L., Filipović M. D., Reid W., Jones P. A., Staveley-Smith L., White G. L., 2004, *MNRAS*, **355**, 44
- Peck A. B., Goss W. M., Dickel H. R., Roelfsema P. R., Kesteven M. J., Dickel J. R., Milne D. K., Points S. D., 1997, *ApJ*, **486**, 329
- Pellegrini E. W., Oey M. S., Winkler P. F., Points S. D., Smith R. C., Jaskot A. E., Zastrow J., 2012, *ApJ*, **755**, 40
- Pennock C. M., et al., 2021, *MNRAS*, **506**, 3540
- Pietrzyński G., et al., 2019, *Nature*, **567**, 200
- Points S. D., Smith R. C., Chu Y. H., 2005, in *American Astronomical Society Meeting Abstracts*. p. 132.11
- Schleicher D. R. G., Beck R., 2013, *A&A*, **556**, A142
- Shain C. A., 1959, in Bracewell R. N., ed., *Vol. 9, URSI Symp. 1: Paris Symposium on Radio Astronomy*. p. 328
- Siejkowski H., Soida M., Chyży K. T., 2018, *A&A*, **611**, A7
- Smith R. C., MCELS Team 1999, in Chu Y.-H., Suntzeff N., Hesser J., Bohlender D., eds, *IAU Symposium Vol. 190, New Views of the Magellanic Clouds*. p. 28
- Smith R. C., Points S. D., Chu Y. H., Winkler P. F., Aguilera C., Leiton R., MCELS Team 2005, in *American Astronomical Society Meeting Abstracts*. p. 25.07
- Stanimirović S., Staveley-Smith L., Jones P. A., 2004, *The Astrophysical Journal*, **604**, 176–186
- Strong A. W., Mattox J. R., 1996, *A&A*, **308**, L21
- Subramanian S., Subramaniam A., 2015, *A&A*, **573**, A135
- Tabatabaei F. S., Beck R., Krügel E., Krause M., Berkhuijsen E. M., Gordon K. D., Menten K. M., 2007, *Astronomy & Astrophysics*, **475**, 133–143
- Tabatabaei F. S., Krause M., Fletcher A., Beck R., 2008, *A&A*, **490**, 1005
- Tabatabaei F. S., et al., 2013a, *Astronomy & Astrophysics*, **552**, A19
- Tabatabaei F. S., Berkhuijsen E. M., Frick P., Beck R., Schinnerer E., 2013b, *A&A*, **557**, A129
- Tabatabaei F. S., et al., 2017, *The Astrophysical Journal*, **836**, 185
- Tabatabaei F. S., Mínguez P., Prieto M. A. A., Fernández-Ontiveros J. A., 2018, *Nature Astronomy*, **2**, 83
- Tingay S. J., et al., 2013, *Publ. Astron. Soc. Australia*, **30**, e007
- Valls-Gabaud D., 1998, *Publ. Astron. Soc. Australia*, **15**, 111
- Vermeij R., van der Hulst J. M., 2002, *A&A*, **391**, 1081
- Vogt F. P. A., Seitzzahl I. R., Dopita M. A., Ghavamian P., 2017, *A&A*, **602**, L4
- Wayth R. B., et al., 2015, *Publ. Astron. Soc. Australia*, **32**, e025

- Weilbacher P. M., Streicher O., Palsa R., 2016, MUSE-DRP: MUSE Data Reduction Pipeline (ascl:1610.004)
- Weingartner J. C., Draine B. T., 2001, *ApJ*, **548**, 296
- Winkler P. F., Smith R. C., Points S. D., MCELS Team 2015, in Points S., Kunder A., eds, *Astronomical Society of the Pacific Conference Series Vol. 491, Fifty Years of Wide Field Studies in the Southern Hemisphere: Resolved Stellar Populations of the Galactic Bulge and Magellanic Clouds*. p. 343
- Wong G. F., Filipovic M. D., Crawford E. J., de Horta A. Y., Galvin T., Draskovic D., Payne J. L., 2011a, *Serbian Astronomical Journal*, **182**, 43
- Wong T., et al., 2011b, *ApJS*, **197**, 16
- Wong T., et al., 2017, *ApJ*, **850**, 139
- Yao J. M., Manchester R. N., Wang N., 2017, *ApJ*, **835**, 29
- de Jong T., Klein U., Wielebinski R., Wunderlich E., 1985, *A&A*, **147**, L6
- van der Kruit P. C., 1971, *A&A*, **15**, 110
- van der Marel R. P., Kallivayalil N., 2014, *ApJ*, **781**, 121

This paper has been typeset from a  $\text{\TeX}/\text{\LaTeX}$  file prepared by the author.